Accompanying material

1. Energy spectra

In figure 1 to 24, the energy spectra are shown for each transmitted pulse through the Fermi-chopper, ranging from approximately 1 to 8 Å. In each plot, the two Multi-Grid detectors (blue and green) and the helium-3 tube (red) are shown overlaid, where the wavelength corresponding to the peak center is stated in the figure title. The spectra from the Multi-Grid detectors are obtained using the same ADC threshold used for the scattering analysis, i.e. 1200 ADC channel. This is to better highlight differences in the peak shoulder region.

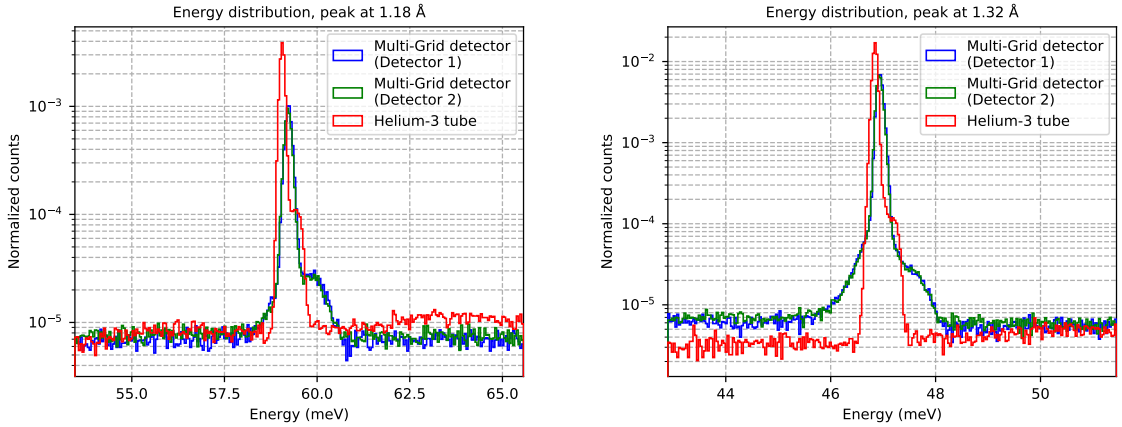

(a) **(b)**

Figure 1: Energy spectra comparing the three detectors used during the measurements, depicting the Multi-Grid detector with non-coated radial blades (blue), with coated radial blades (green) and the helium-3 tube (red). The number of counts are normalized by beam monitor data.

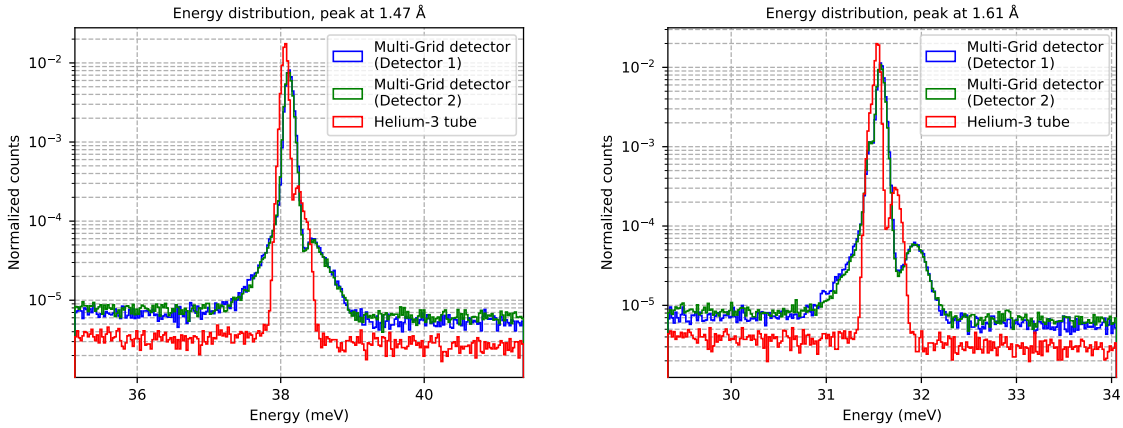

(a) **(b)**

Figure 2: Energy spectra comparing the three detectors used during the measurements, depicting the Multi-Grid detector with non-coated radial blades (blue), with coated radial blades (green) and the helium-3 tube (red). The number of counts are normalized by beam monitor data.

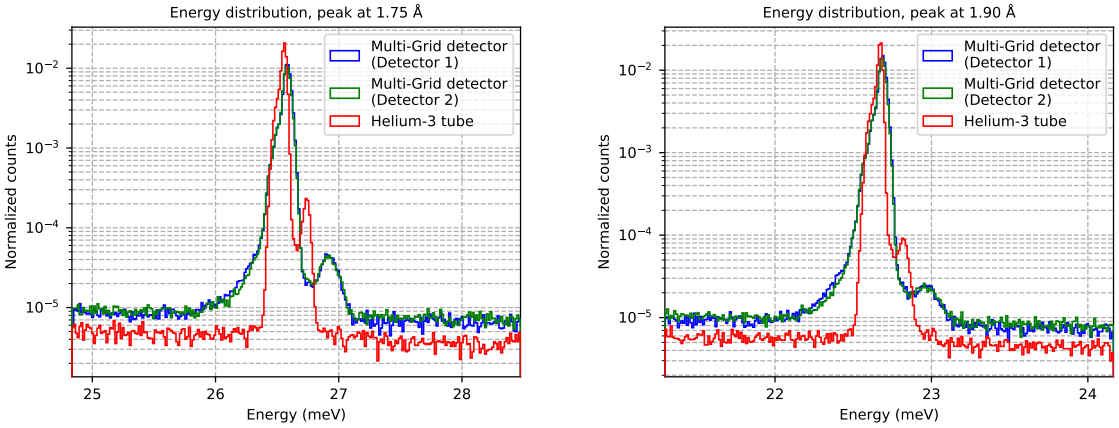

(a) **(b)**

Figure 3: Energy spectra comparing the three detectors used during the measurements, depicting the Multi-Grid detector with non-coated radial blades (blue), with coated radial blades (green) and the helium-3 tube (red). The number of counts are normalized by beam monitor data.

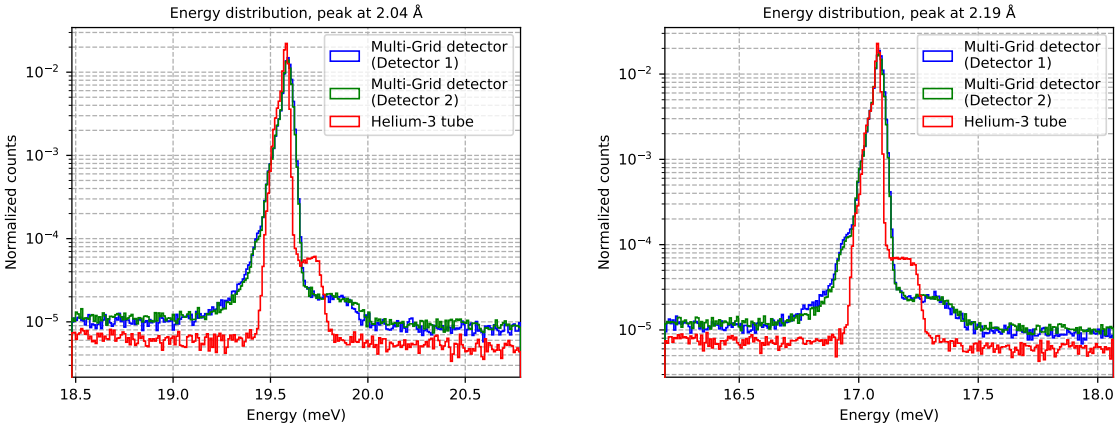

(a) **(b)**

Figure 4: Energy spectra comparing the three detectors used during the measurements, depicting the Multi-Grid detector with non-coated radial blades (blue), with coated radial blades (green) and the helium-3 tube (red). The number of counts are normalized by beam monitor data.

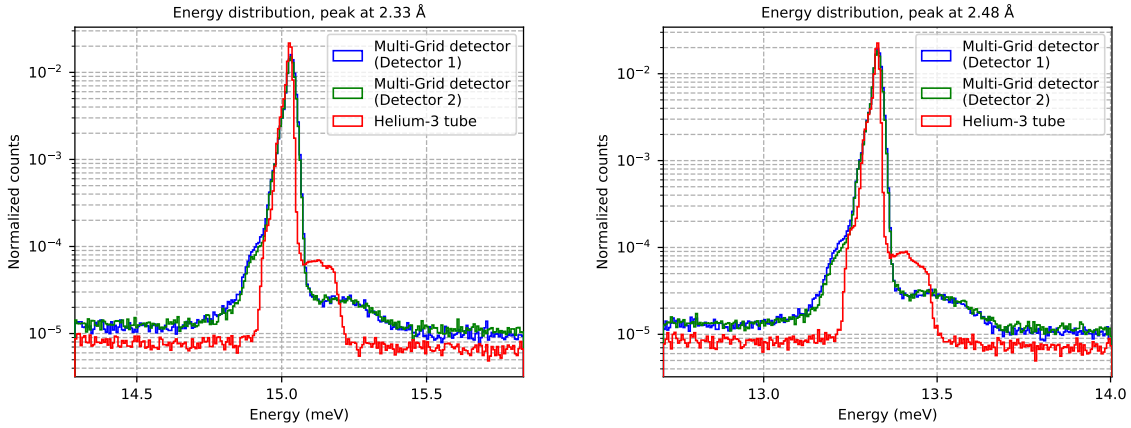

(a) **(b)**

Figure 5: Energy spectra comparing the three detectors used during the measurements, depicting the Multi-Grid detector with non-coated radial blades (blue), with coated radial blades (green) and the helium-3 tube (red). The number of counts are normalized by beam monitor data.

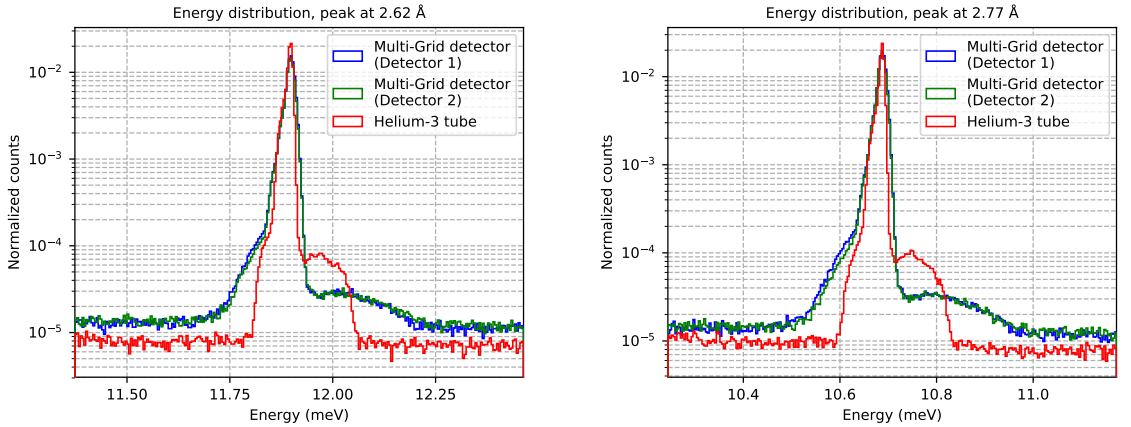

(a) **(b)**

Figure 6: Energy spectra comparing the three detectors used during the measurements, depicting the Multi-Grid detector with non-coated radial blades (blue), with coated radial blades (green) and the helium-3 tube (red). The number of counts are normalized by beam monitor data.

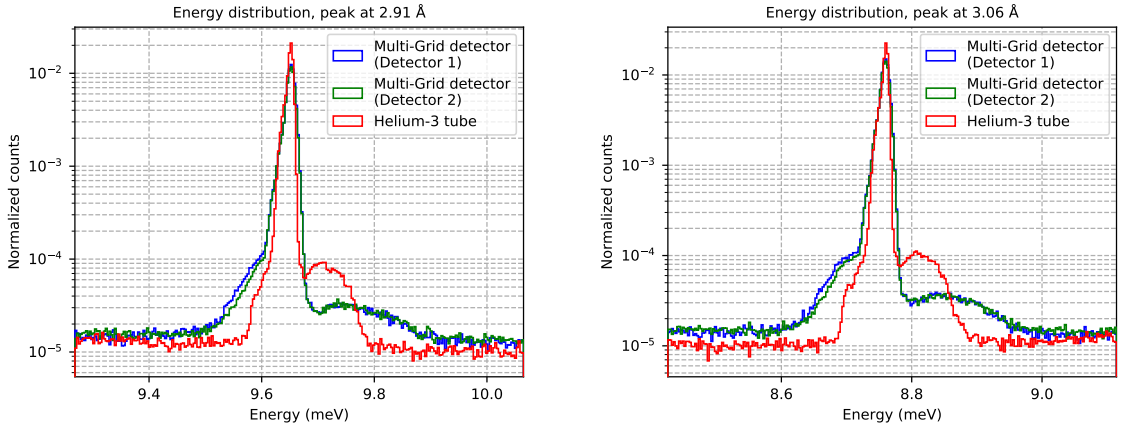

(a) **(b)**

Figure 7: Energy spectra comparing the three detectors used during the measurements, depicting the Multi-Grid detector with non-coated radial blades (blue), with coated radial blades (green) and the helium-3 tube (red). The number of counts are normalized by beam monitor data.

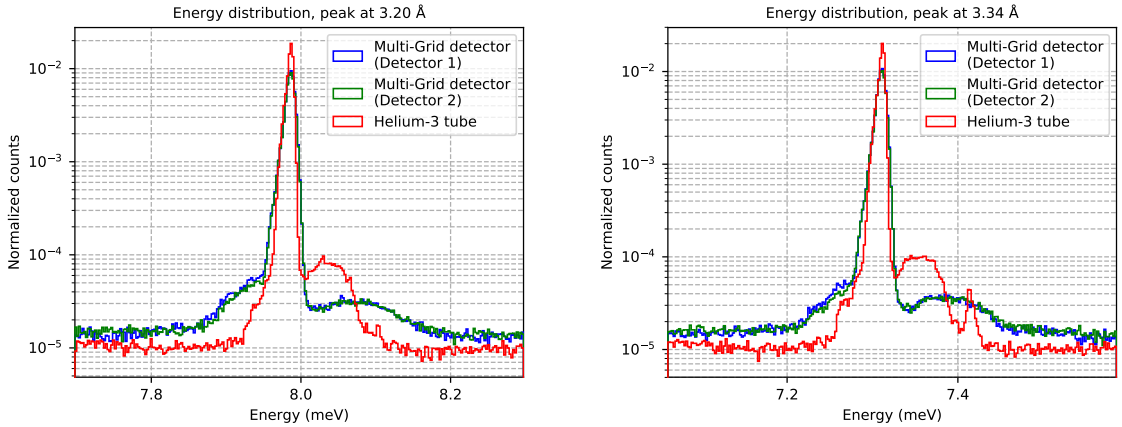

(a) **(b)**

Figure 8: Energy spectra comparing the three detectors used during the measurements, depicting the Multi-Grid detector with non-coated radial blades (blue), with coated radial blades (green) and the helium-3 tube (red). The number of counts are normalized by beam monitor data.

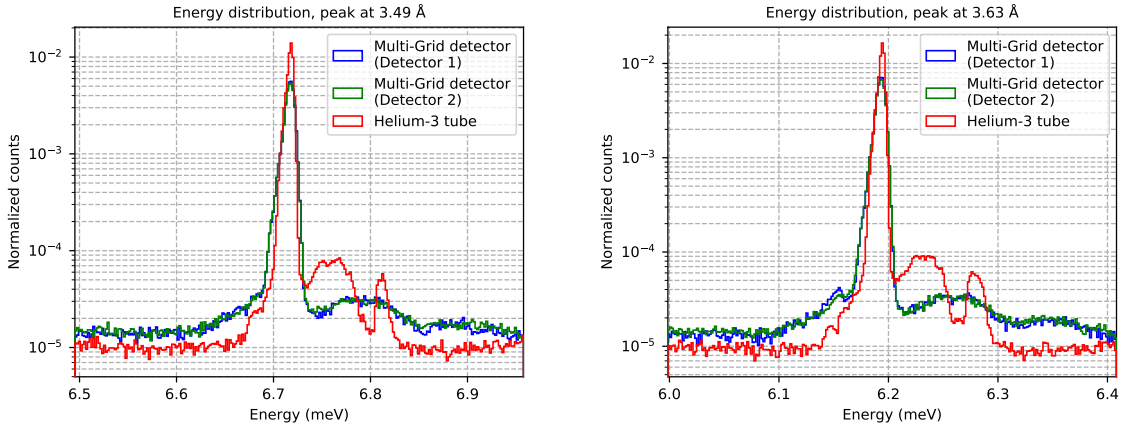

(a) **(b)**

Figure 9: Energy spectra comparing the three detectors used during the measurements, depicting the Multi-Grid detector with non-coated radial blades (blue), with coated radial blades (green) and the helium-3 tube (red). The number of counts are normalized by beam monitor data.

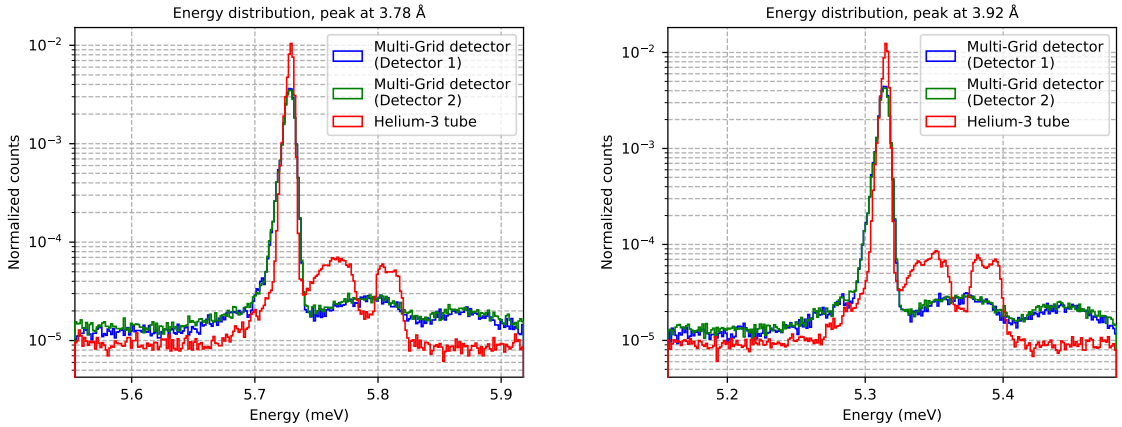

(a) **(b)**

Figure 10: Energy spectra comparing the three detectors used during the measurements, depicting the Multi-Grid detector with non-coated radial blades (blue), with coated radial blades (green) and the helium-3 tube (red). The number of counts are normalized by beam monitor data.

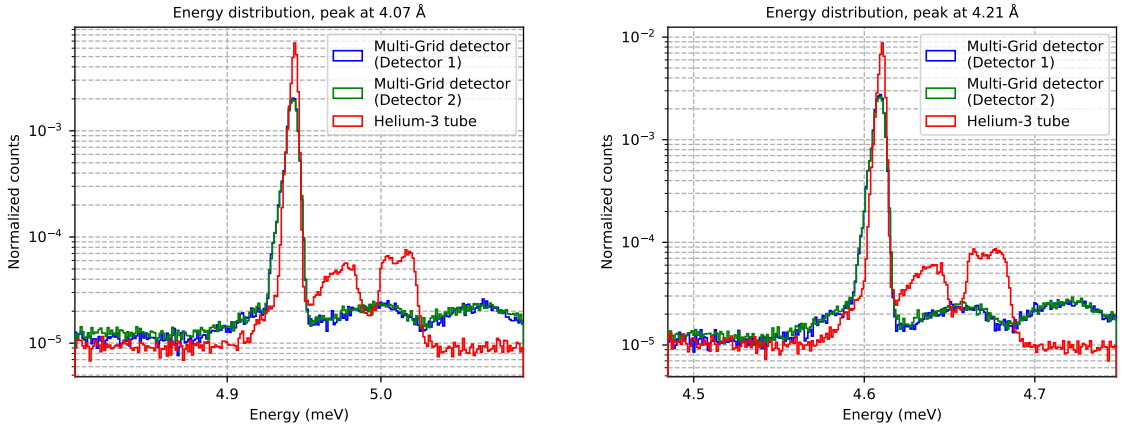

(a) **(b)**

Figure 11: Energy spectra comparing the three detectors used during the measurements, depicting the Multi-Grid detector with non-coated radial blades (blue), with coated radial blades (green) and the helium-3 tube (red). The number of counts are normalized by beam monitor data.

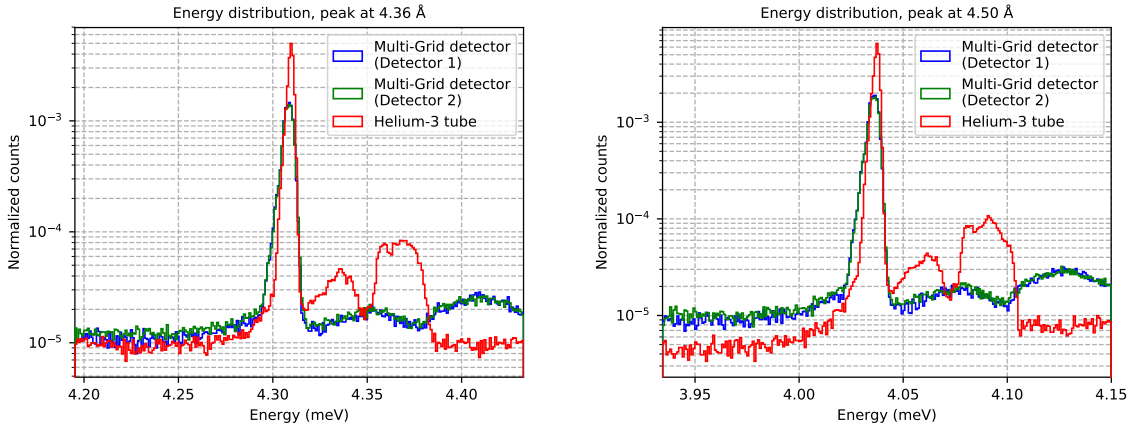

(a) **(b)**

Figure 12: Energy spectra comparing the three detectors used during the measurements, depicting the Multi-Grid detector with non-coated radial blades (blue), with coated radial blades (green) and the helium-3 tube (red). The number of counts are normalized by beam monitor data.

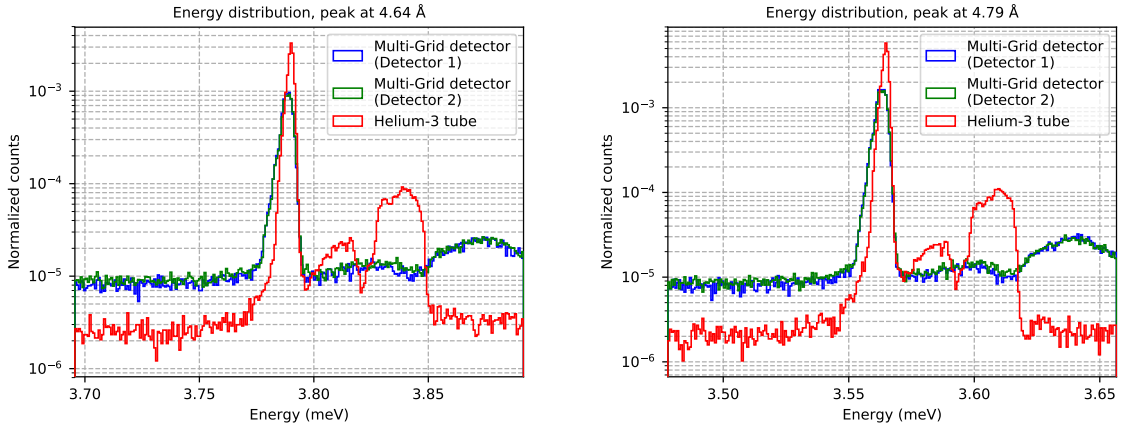

(a) **(b)**

Figure 13: Energy spectra comparing the three detectors used during the measurements, depicting the Multi-Grid detector with non-coated radial blades (blue), with coated radial blades (green) and the helium-3 tube (red). The number of counts are normalized by beam monitor data.

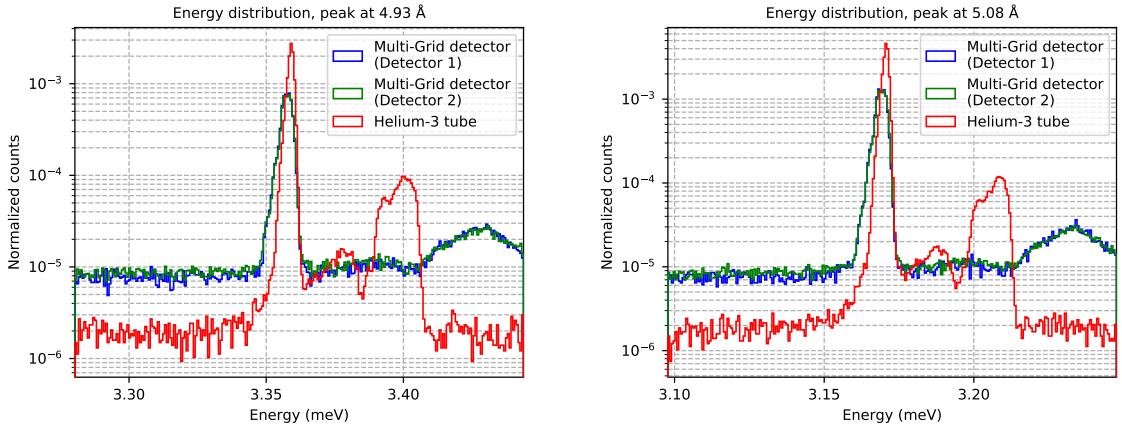

(a) **(b)**

Figure 14: Energy spectra comparing the three detectors used during the measurements, depicting the Multi-Grid detector with non-coated radial blades (blue), with coated radial blades (green) and the helium-3 tube (red). The number of counts are normalized by beam monitor data.

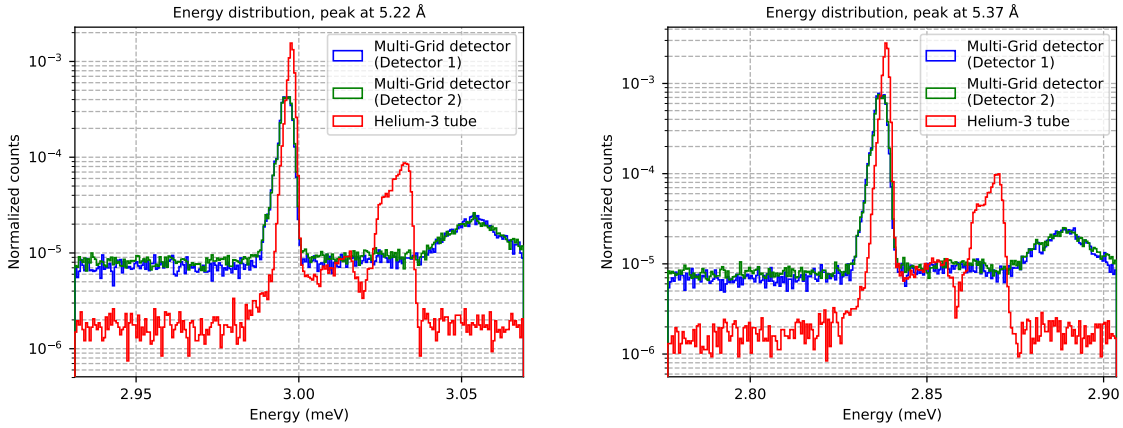

(a) **(b)**

Figure 15: Energy spectra comparing the three detectors used during the measurements, depicting the Multi-Grid detector with non-coated radial blades (blue), with coated radial blades (green) and the helium-3 tube (red). The number of counts are normalized by beam monitor data.

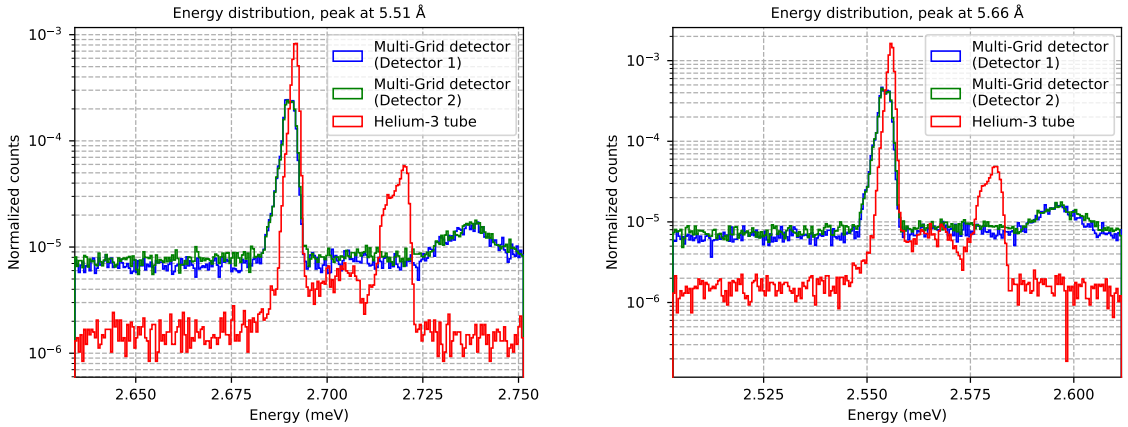

(a) **(b)**

Figure 16: Energy spectra comparing the three detectors used during the measurements, depicting the Multi-Grid detector with non-coated radial blades (blue), with coated radial blades (green) and the helium-3 tube (red). The number of counts are normalized by beam monitor data.

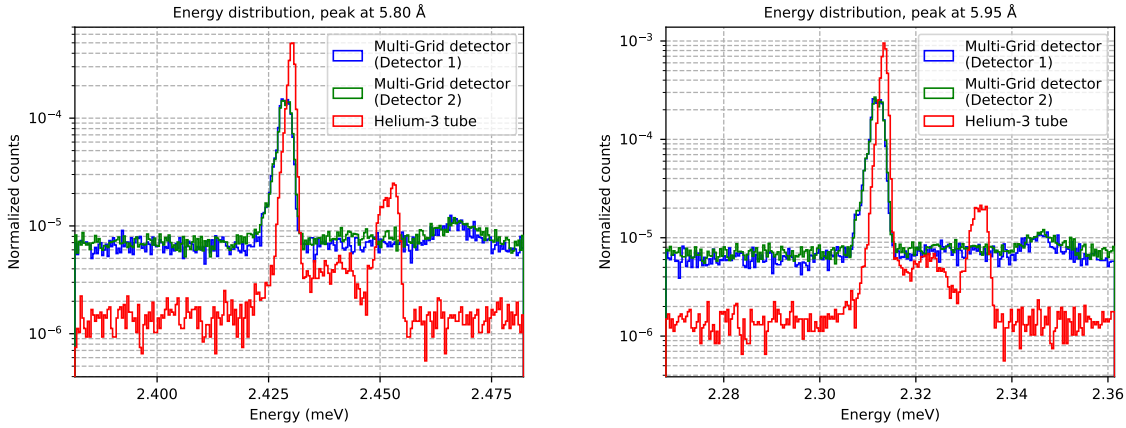

(a) **(b)**

Figure 17: Energy spectra comparing the three detectors used during the measurements, depicting the Multi-Grid detector with non-coated radial blades (blue), with coated radial blades (green) and the helium-3 tube (red). The number of counts are normalized by beam monitor data.

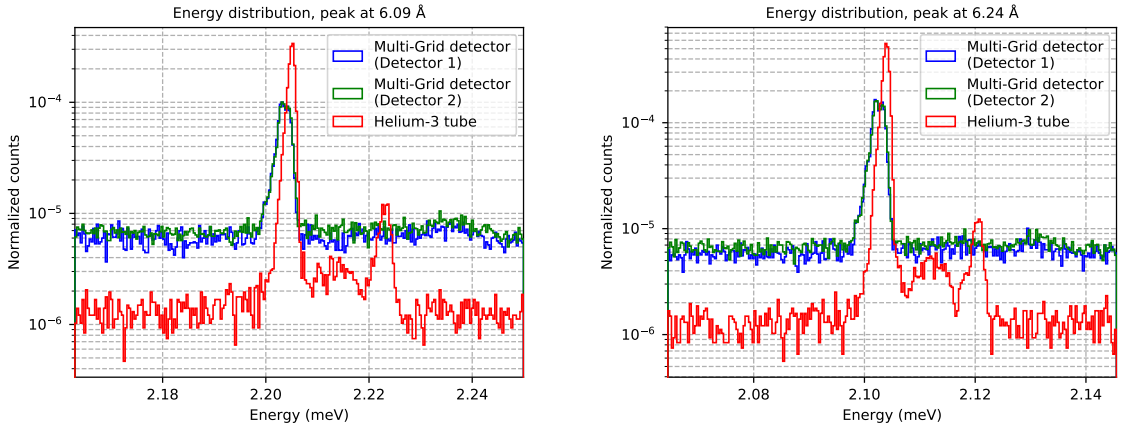

(a) **(b)**

Figure 18: Energy spectra comparing the three detectors used during the measurements, depicting the Multi-Grid detector with non-coated radial blades (blue), with coated radial blades (green) and the helium-3 tube (red). The number of counts are normalized by beam monitor data.

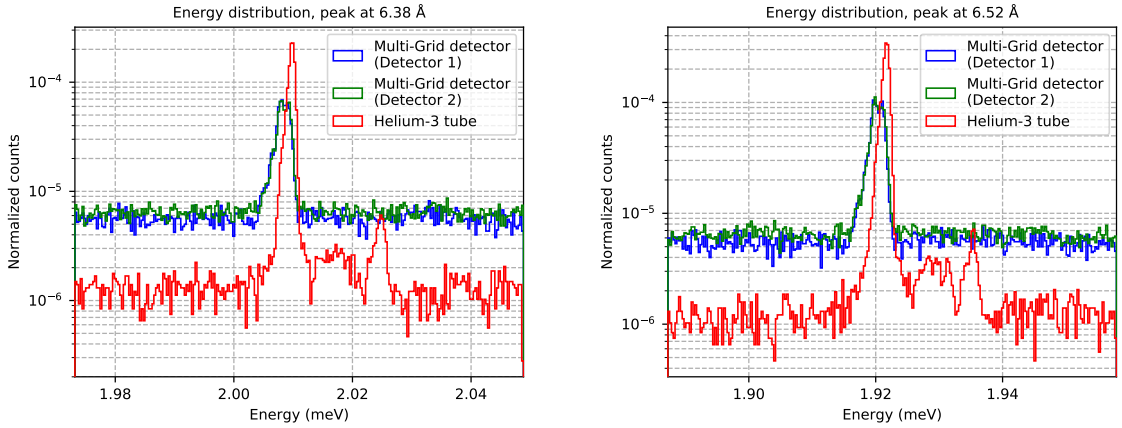

(a) **(b)**

Figure 19: Energy spectra comparing the three detectors used during the measurements, depicting the Multi-Grid detector with non-coated radial blades (blue), with coated radial blades (green) and the helium-3 tube (red). The number of counts are normalized by beam monitor data.

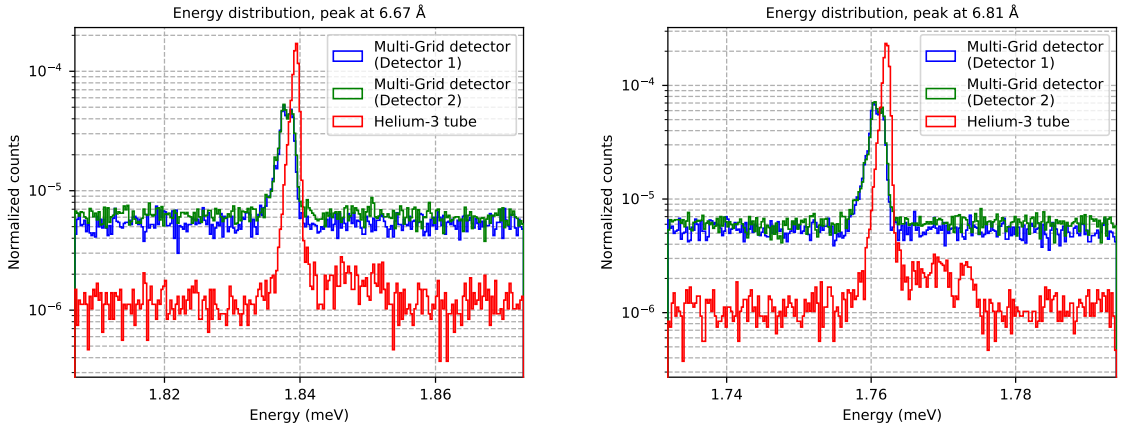

(a) **(b)**

Figure 20: Energy spectra comparing the three detectors used during the measurements, depicting the Multi-Grid detector with non-coated radial blades (blue), with coated radial blades (green) and the helium-3 tube (red). The number of counts are normalized by beam monitor data.

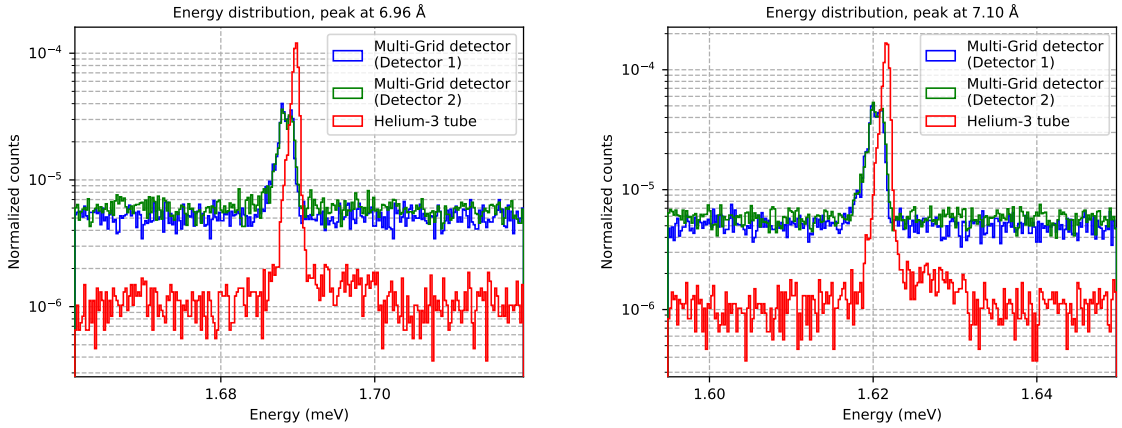

(a) **(b)**

Figure 21: Energy spectra comparing the three detectors used during the measurements, depicting the Multi-Grid detector with non-coated radial blades (blue), with coated radial blades (green) and the helium-3 tube (red). The number of counts are normalized by beam monitor data.

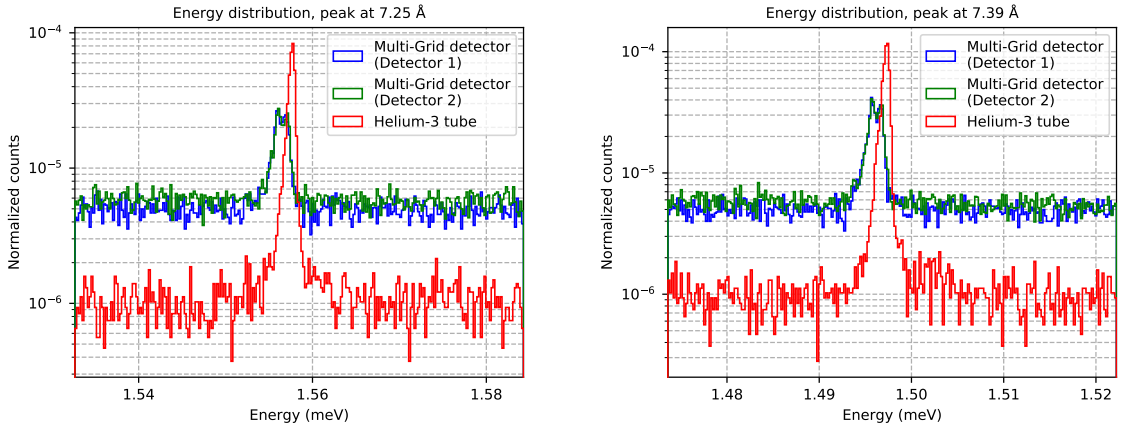

(a) **(b)**

Figure 22: Energy spectra comparing the three detectors used during the measurements, depicting the Multi-Grid detector with non-coated radial blades (blue), with coated radial blades (green) and the helium-3 tube (red). The number of counts are normalized by beam monitor data.

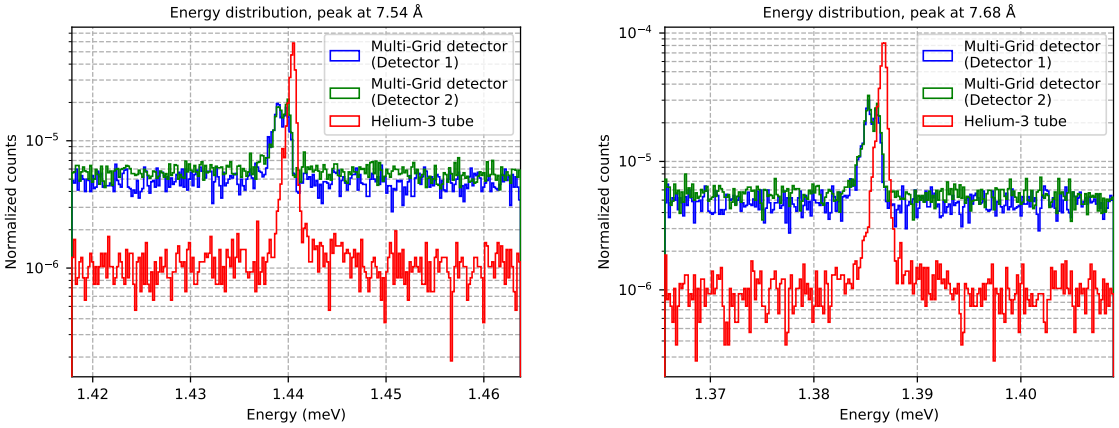

(a) **(b)**

Figure 23: Energy spectra comparing the three detectors used during the measurements, depicting the Multi-Grid detector with non-coated radial blades (blue), with coated radial blades (green) and the helium-3 tube (red). The number of counts are normalized by beam monitor data.

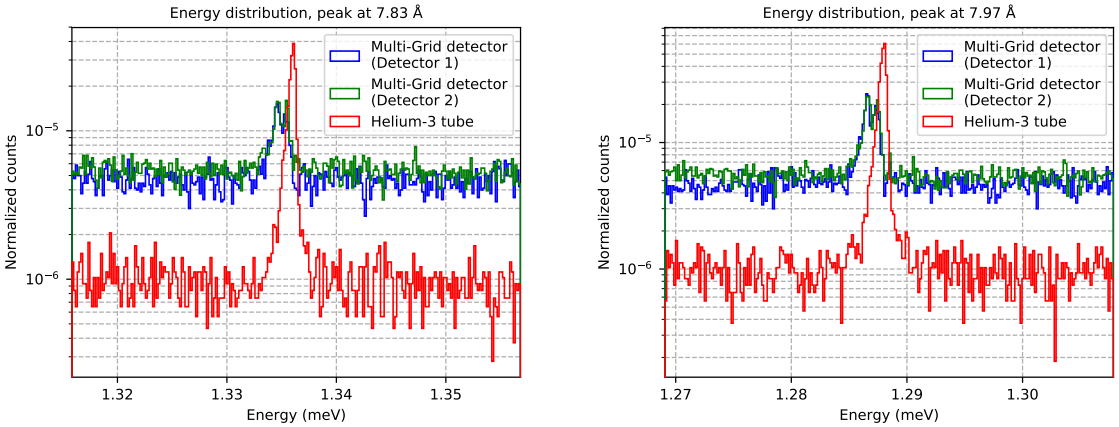

(a) **(b)**

Figure 24: Energy spectra comparing the three detectors used during the measurements, depicting the Multi-Grid detector with non-coated radial blades (blue), with coated radial blades (green) and the helium-3 tube (red). The number of counts are normalized by beam monitor data.

2. Internal neutron scattering

In figure 25 to 63, the two Multi-Grid detectors, non-coated radial blades (blue) and coated radial blades (green), are compared in terms of internal scattering. Each figure presents a peak transmitted through the Fermi-chopper, ranging from approximately 1 to 7 Å. The red histograms are based on statistics from the beam periphery regions. Note that the wavelength corresponding to the peak center is stated in the figure titles.

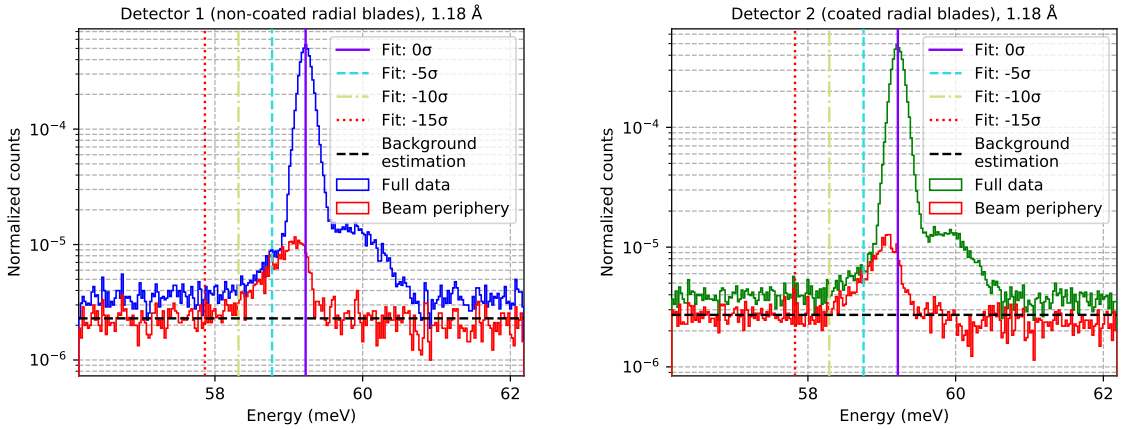

Figure 25: Effect on peak shape by internally scattered neutrons. Histograms from the full data in Detector 1 (blue) and Detector 2 (green) are compared to data where the direct beam is removed (red). The background estimation is shown as a black horizontal line. The integration limits are presented as vertical lines, including 0σ (solid), -5σ (dashed), -10σ (dash-dotted), and -15σ (dotted). The parameter σ is the standard-deviation around the peak center, calculated using a Gaussian fit. The number of counts are normalized by beam monitor data.

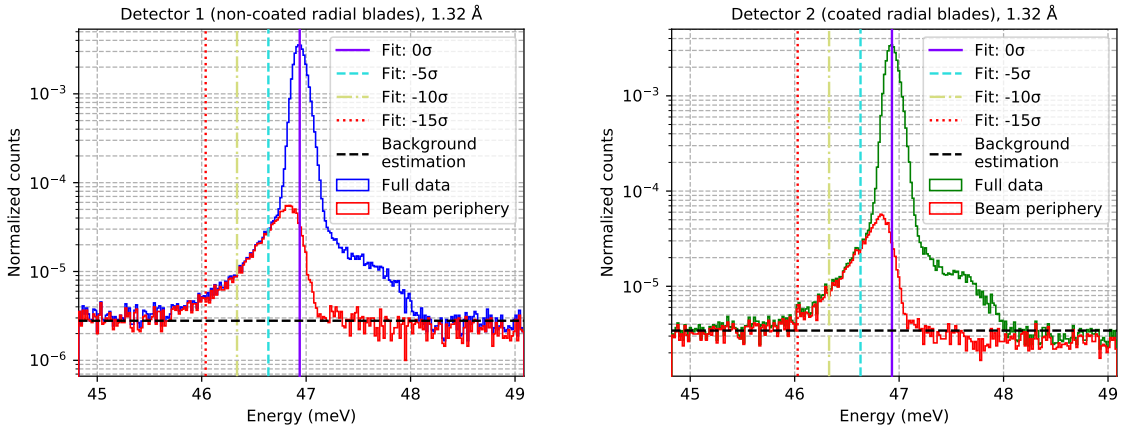

(a) **(b)**

Figure 26: Effect on peak shape by internally scattered neutrons. Histograms from the full data in Detector 1 (blue) and Detector 2 (green) are compared to data where the direct beam is removed (red). The background estimation is shown as a black horizontal line. The integration limits are presented as vertical lines, including 0σ (solid), -5σ (dashed), -10σ (dash-dotted), and -15σ (dotted). The parameter σ is the standard-deviation around the peak center, calculated using a Gaussian fit. The number of counts are normalized by beam monitor data.

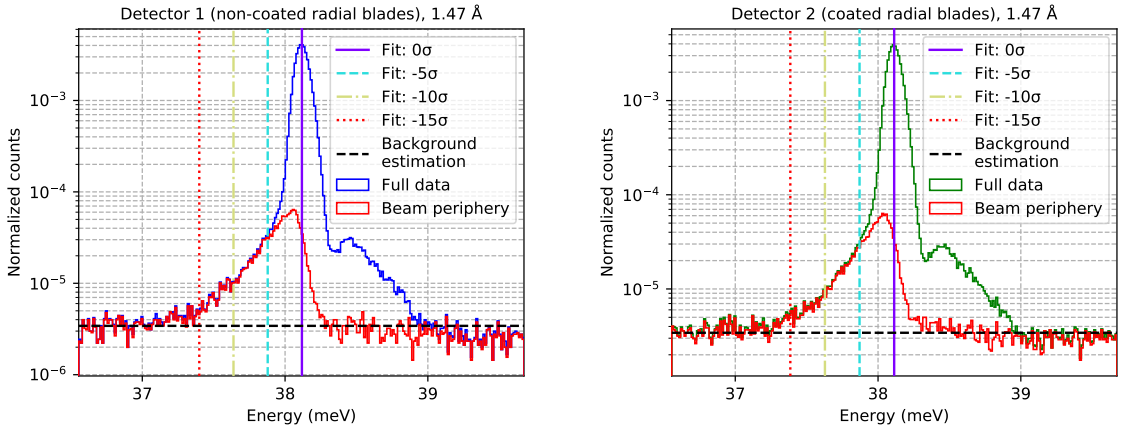

(a) **(b)**

Figure 27: Effect on peak shape by internally scattered neutrons. Histograms from the full data in Detector 1 (blue) and Detector 2 (green) are compared to data where the direct beam is removed (red). The background estimation is shown as a black horizontal line. The integration limits are presented as vertical lines, including 0σ (solid), -5σ (dashed), -10σ (dash-dotted), and -15σ (dotted). The parameter σ is the standard-deviation around the peak center, calculated using a Gaussian fit. The number of counts are normalized by beam monitor data.

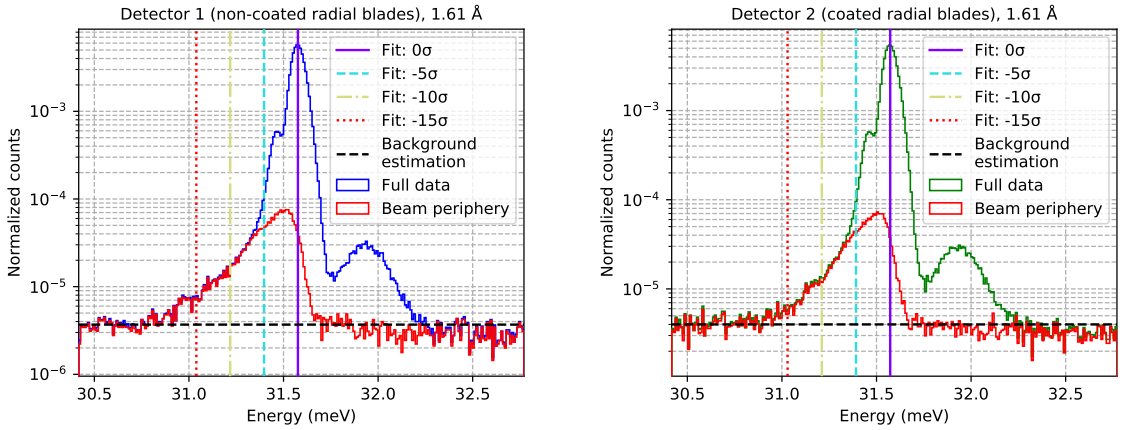

Figure 28: Effect on peak shape by internally scattered neutrons. Histograms from the full data in Detector 1 (blue) and Detector 2 (green) are compared to data where the direct beam is removed (red). The background estimation is shown as a black horizontal line. The integration limits are presented as vertical lines, including 0σ (solid), -5σ (dashed), -10σ (dash-dotted), and -15σ (dotted). The parameter σ is the standard-deviation around the peak center, calculated using a Gaussian fit. The number of counts are normalized by beam monitor data.

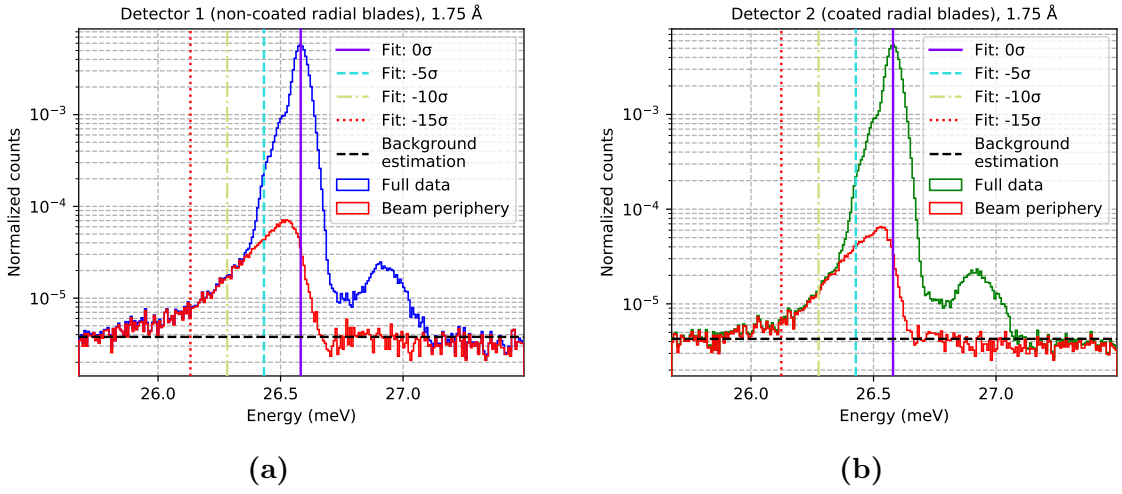

Figure 29: Effect on peak shape by internally scattered neutrons. Histograms from the full data in Detector 1 (blue) and Detector 2 (green) are compared to data where the direct beam is removed (red). The background estimation is shown as a black horizontal line. The integration limits are presented as vertical lines, including 0σ (solid), -5σ (dashed), -10σ (dash-dotted), and -15σ (dotted). The parameter σ is the standard-deviation around the peak center, calculated using a Gaussian fit. The number of counts are normalized by beam monitor data.

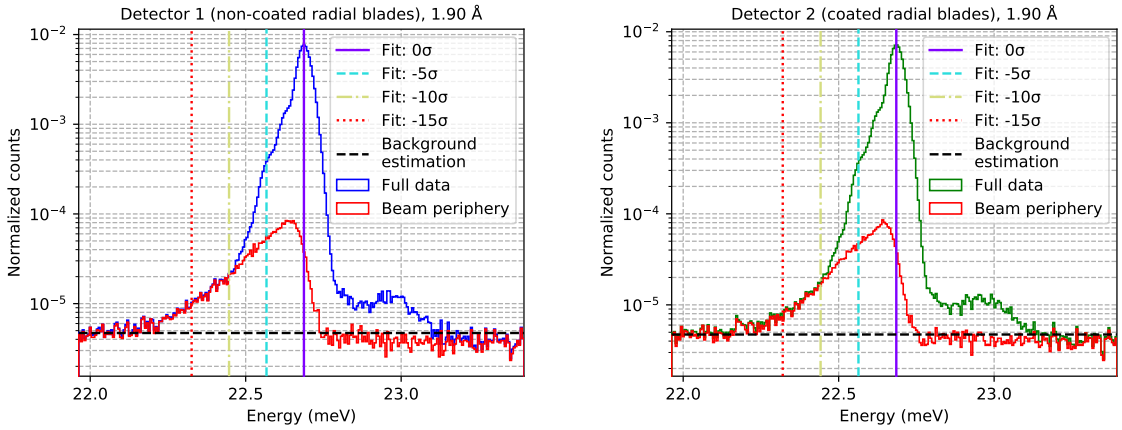

(a) **(b)**

Figure 30: Effect on peak shape by internally scattered neutrons. Histograms from the full data in Detector 1 (blue) and Detector 2 (green) are compared to data where the direct beam is removed (red). The background estimation is shown as a black horizontal line. The integration limits are presented as vertical lines, including 0σ (solid), -5σ (dashed), -10σ (dash-dotted), and -15σ (dotted). The parameter σ is the standard-deviation around the peak center, calculated using a Gaussian fit. The number of counts are normalized by beam monitor data.

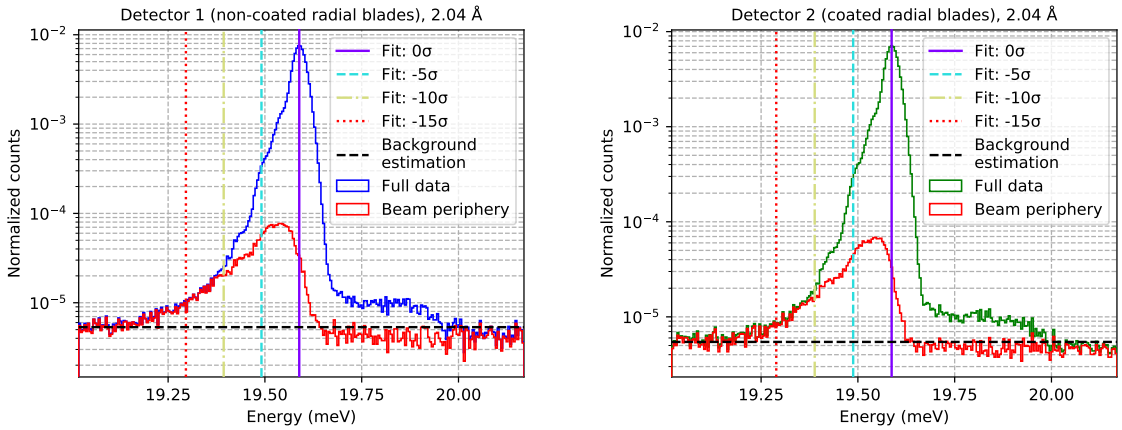

(a) **(b)**

Figure 31: Effect on peak shape by internally scattered neutrons. Histograms from the full data in Detector 1 (blue) and Detector 2 (green) are compared to data where the direct beam is removed (red). The background estimation is shown as a black horizontal line. The integration limits are presented as vertical lines, including 0σ (solid), -5σ (dashed), -10σ (dash-dotted), and -15σ (dotted). The parameter σ is the standard-deviation around the peak center, calculated using a Gaussian fit. The number of counts are normalized by beam monitor data.

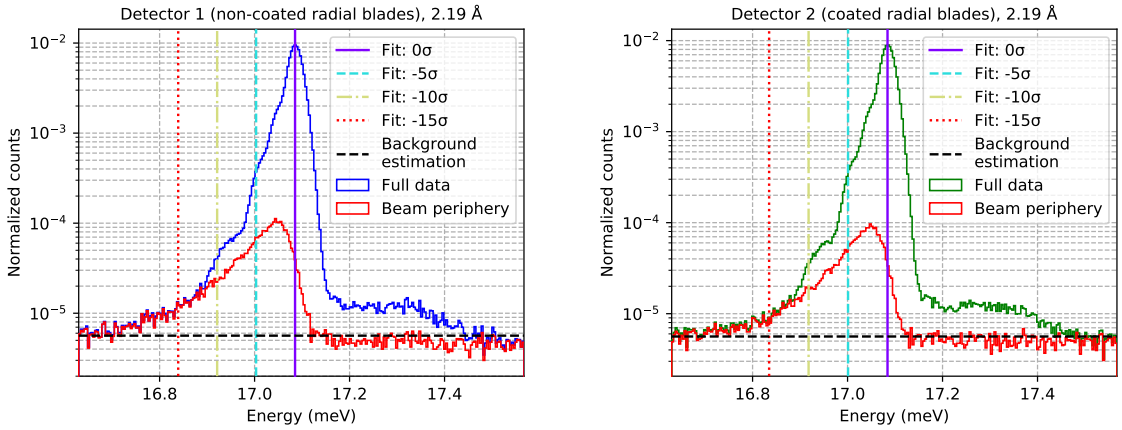

(a) **(b)**

Figure 32: Effect on peak shape by internally scattered neutrons. Histograms from the full data in Detector 1 (blue) and Detector 2 (green) are compared to data where the direct beam is removed (red). The background estimation is shown as a black horizontal line. The integration limits are presented as vertical lines, including 0σ (solid), -5σ (dashed), -10σ (dash-dotted), and -15σ (dotted). The parameter σ is the standard-deviation around the peak center, calculated using a Gaussian fit. The number of counts are normalized by beam monitor data.

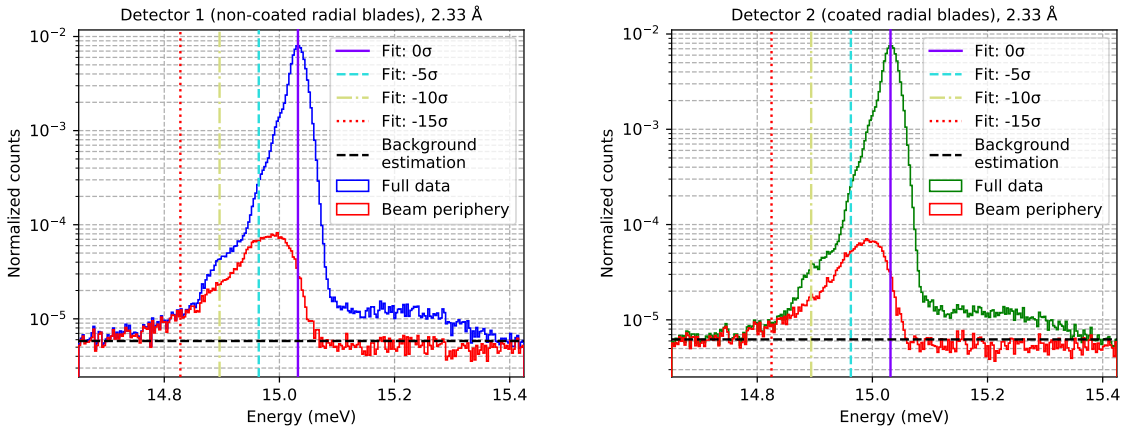

(a) **(b)**

Figure 33: Effect on peak shape by internally scattered neutrons. Histograms from the full data in Detector 1 (blue) and Detector 2 (green) are compared to data where the direct beam is removed (red). The background estimation is shown as a black horizontal line. The integration limits are presented as vertical lines, including 0σ (solid), -5σ (dashed), -10σ (dash-dotted), and -15σ (dotted). The parameter σ is the standard-deviation around the peak center, calculated using a Gaussian fit. The number of counts are normalized by beam monitor data.

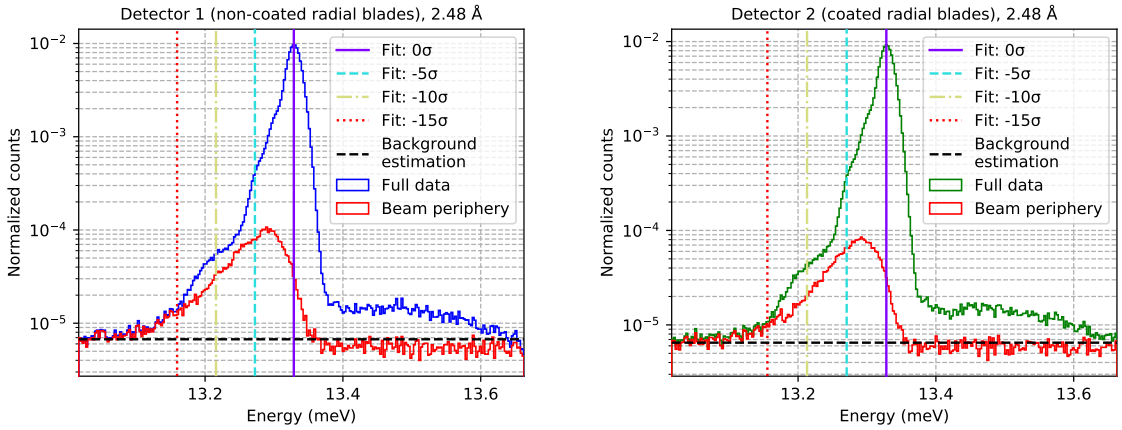

(a) **(b)**

Figure 34: Effect on peak shape by internally scattered neutrons. Histograms from the full data in Detector 1 (blue) and Detector 2 (green) are compared to data where the direct beam is removed (red). The background estimation is shown as a black horizontal line. The integration limits are presented as vertical lines, including 0σ (solid), -5σ (dashed), -10σ (dash-dotted), and -15σ (dotted). The parameter σ is the standard-deviation around the peak center, calculated using a Gaussian fit. The number of counts are normalized by beam monitor data.

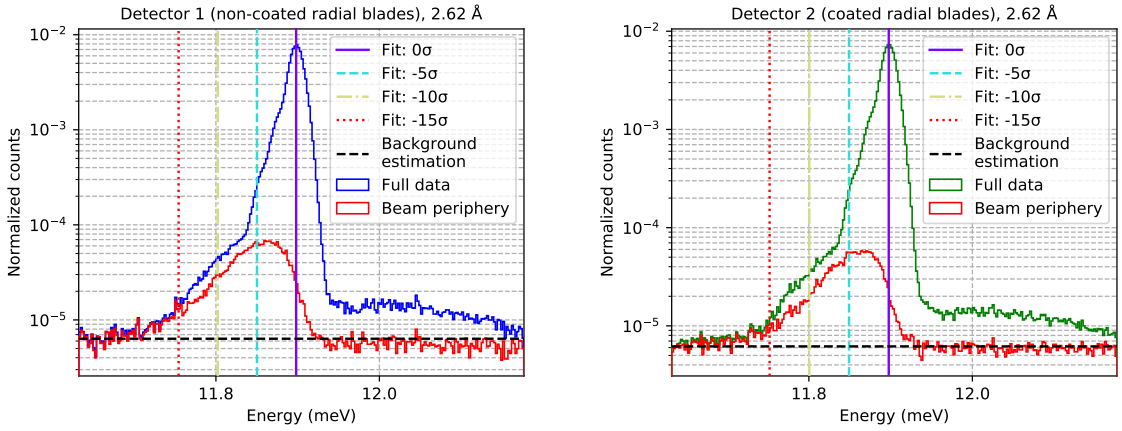

(a) **(b)**

Figure 35: Effect on peak shape by internally scattered neutrons. Histograms from the full data in Detector 1 (blue) and Detector 2 (green) are compared to data where the direct beam is removed (red). The background estimation is shown as a black horizontal line. The integration limits are presented as vertical lines, including 0σ (solid), -5σ (dashed), -10σ (dash-dotted), and -15σ (dotted). The parameter σ is the standard-deviation around the peak center, calculated using a Gaussian fit. The number of counts are normalized by beam monitor data.

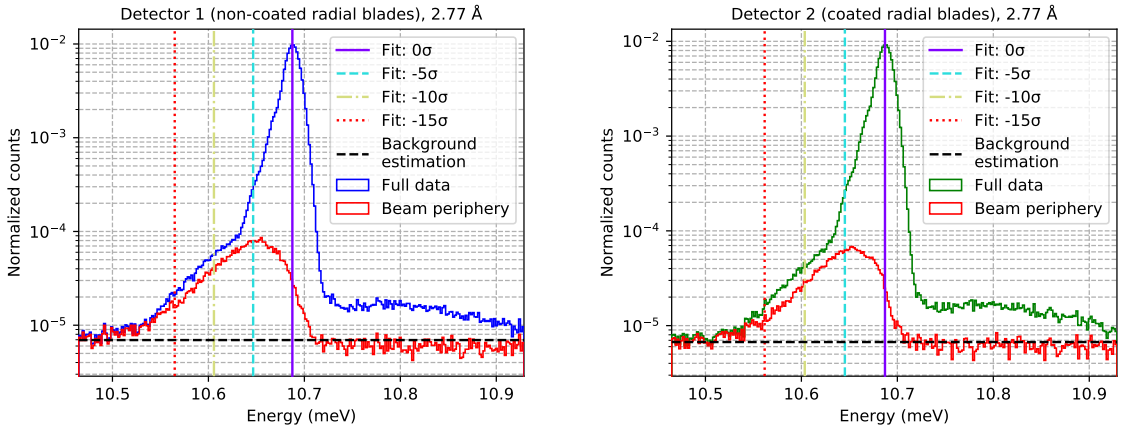

(a) **(b)**

Figure 36: Effect on peak shape by internally scattered neutrons. Histograms from the full data in Detector 1 (blue) and Detector 2 (green) are compared to data where the direct beam is removed (red). The background estimation is shown as a black horizontal line. The integration limits are presented as vertical lines, including 0σ (solid), -5σ (dashed), -10σ (dash-dotted), and -15σ (dotted). The parameter σ is the standard-deviation around the peak center, calculated using a Gaussian fit. The number of counts are normalized by beam monitor data.

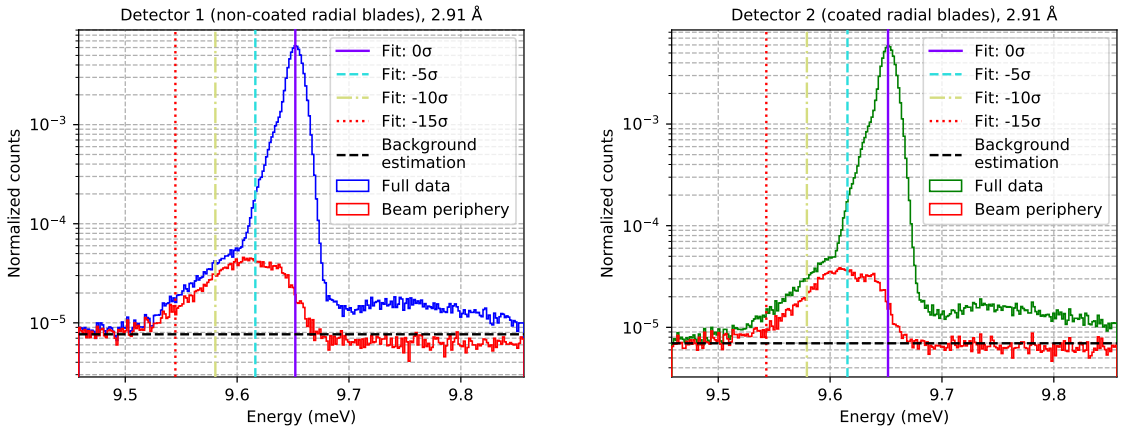

(a) **(b)**

Figure 37: Effect on peak shape by internally scattered neutrons. Histograms from the full data in Detector 1 (blue) and Detector 2 (green) are compared to data where the direct beam is removed (red). The background estimation is shown as a black horizontal line. The integration limits are presented as vertical lines, including 0σ (solid), -5σ (dashed), -10σ (dash-dotted), and -15σ (dotted). The parameter σ is the standard-deviation around the peak center, calculated using a Gaussian fit. The number of counts are normalized by beam monitor data.

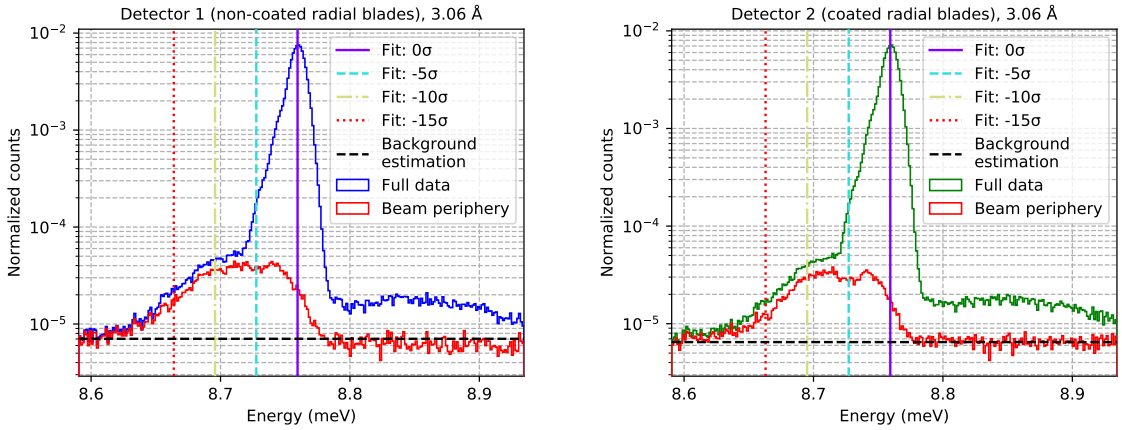

(a) **(b)**

Figure 38: Effect on peak shape by internally scattered neutrons. Histograms from the full data in Detector 1 (blue) and Detector 2 (green) are compared to data where the direct beam is removed (red). The background estimation is shown as a black horizontal line. The integration limits are presented as vertical lines, including 0σ (solid), -5σ (dashed), -10σ (dash-dotted), and -15σ (dotted). The parameter σ is the standard-deviation around the peak center, calculated using a Gaussian fit. The number of counts are normalized by beam monitor data.

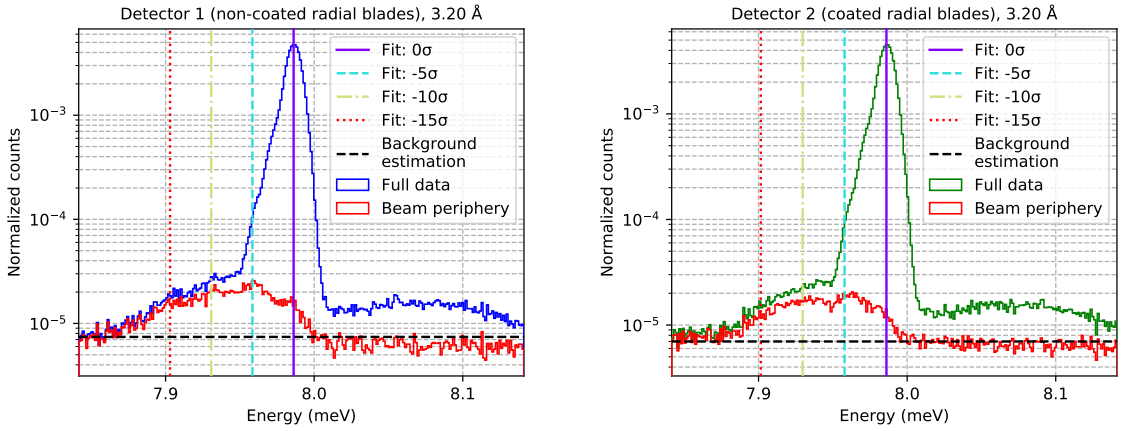

(a) **(b)**

Figure 39: Effect on peak shape by internally scattered neutrons. Histograms from the full data in Detector 1 (blue) and Detector 2 (green) are compared to data where the direct beam is removed (red). The background estimation is shown as a black horizontal line. The integration limits are presented as vertical lines, including 0σ (solid), -5σ (dashed), -10σ (dash-dotted), and -15σ (dotted). The parameter σ is the standard-deviation around the peak center, calculated using a Gaussian fit. The number of counts are normalized by beam monitor data.

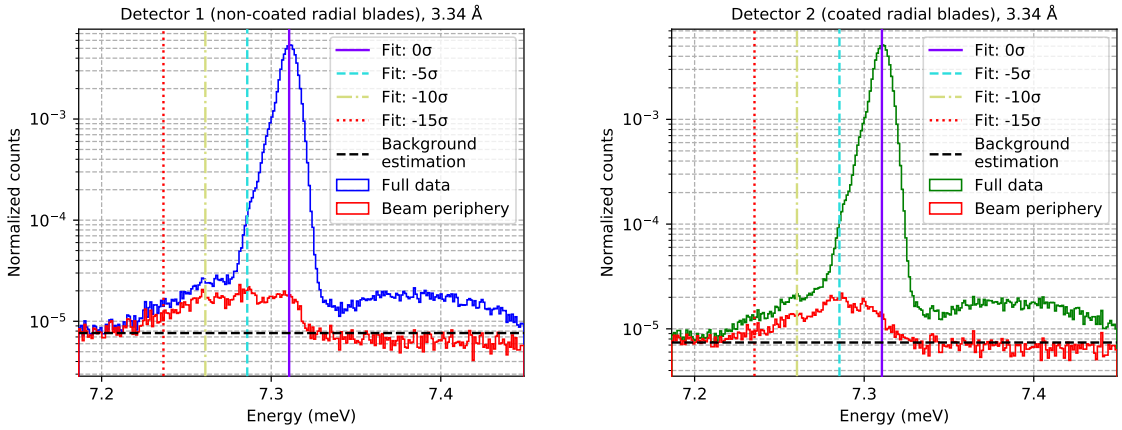

Figure 40: Effect on peak shape by internally scattered neutrons. Histograms from the full data in Detector 1 (blue) and Detector 2 (green) are compared to data where the direct beam is removed (red). The background estimation is shown as a black horizontal line. The integration limits are presented as vertical lines, including 0σ (solid), -5σ (dashed), -10σ (dash-dotted), and -15σ (dotted). The parameter σ is the standard-deviation around the peak center, calculated using a Gaussian fit. The number of counts are normalized by beam monitor data.

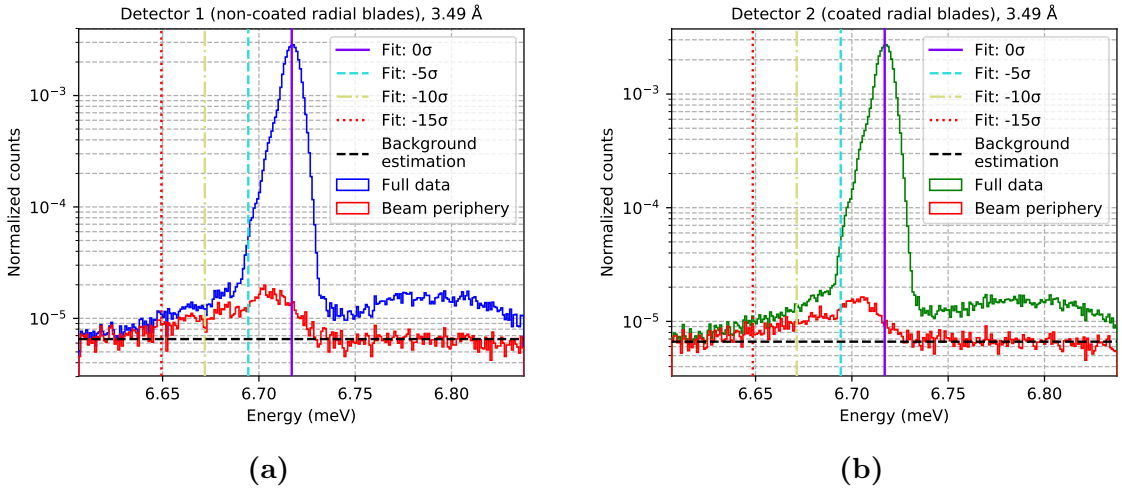

Figure 41: Effect on peak shape by internally scattered neutrons. Histograms from the full data in Detector 1 (blue) and Detector 2 (green) are compared to data where the direct beam is removed (red). The background estimation is shown as a black horizontal line. The integration limits are presented as vertical lines, including 0σ (solid), -5σ (dashed), -10σ (dash-dotted), and -15σ (dotted). The parameter σ is the standard-deviation around the peak center, calculated using a Gaussian fit. The number of counts are normalized by beam monitor data.

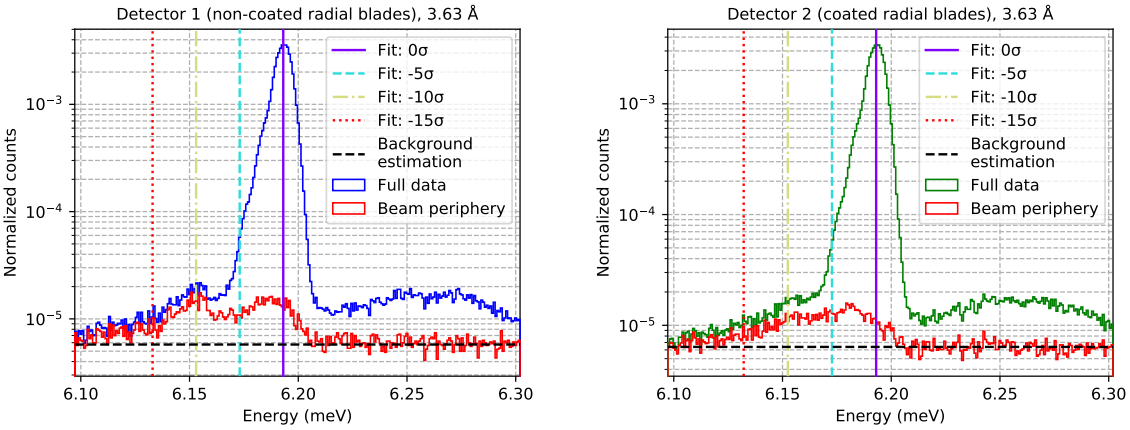

(a) **(b)**

Figure 42: Effect on peak shape by internally scattered neutrons. Histograms from the full data in Detector 1 (blue) and Detector 2 (green) are compared to data where the direct beam is removed (red). The background estimation is shown as a black horizontal line. The integration limits are presented as vertical lines, including 0σ (solid), -5σ (dashed), -10σ (dash-dotted), and -15σ (dotted). The parameter σ is the standard-deviation around the peak center, calculated using a Gaussian fit. The number of counts are normalized by beam monitor data.

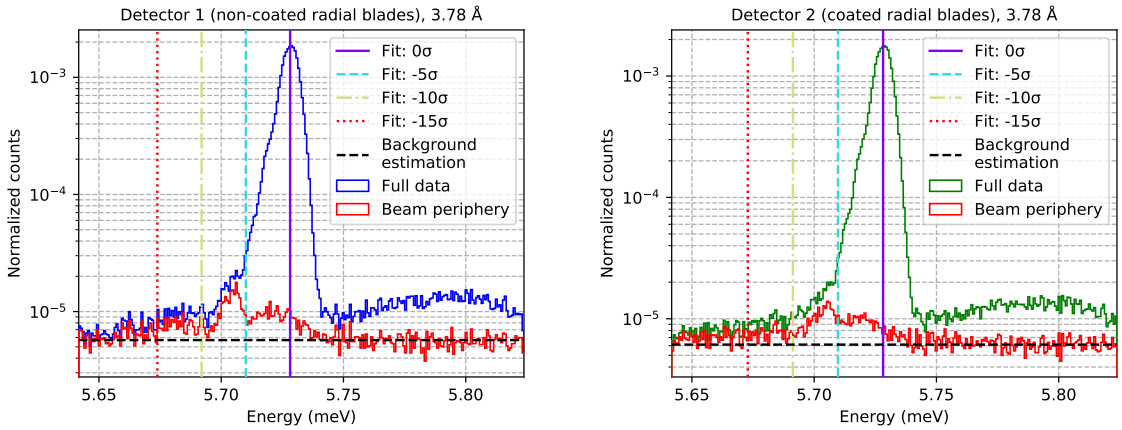

(a) **(b)**

Figure 43: Effect on peak shape by internally scattered neutrons. Histograms from the full data in Detector 1 (blue) and Detector 2 (green) are compared to data where the direct beam is removed (red). The background estimation is shown as a black horizontal line. The integration limits are presented as vertical lines, including 0σ (solid), -5σ (dashed), -10σ (dash-dotted), and -15σ (dotted). The parameter σ is the standard-deviation around the peak center, calculated using a Gaussian fit. The number of counts are normalized by beam monitor data.

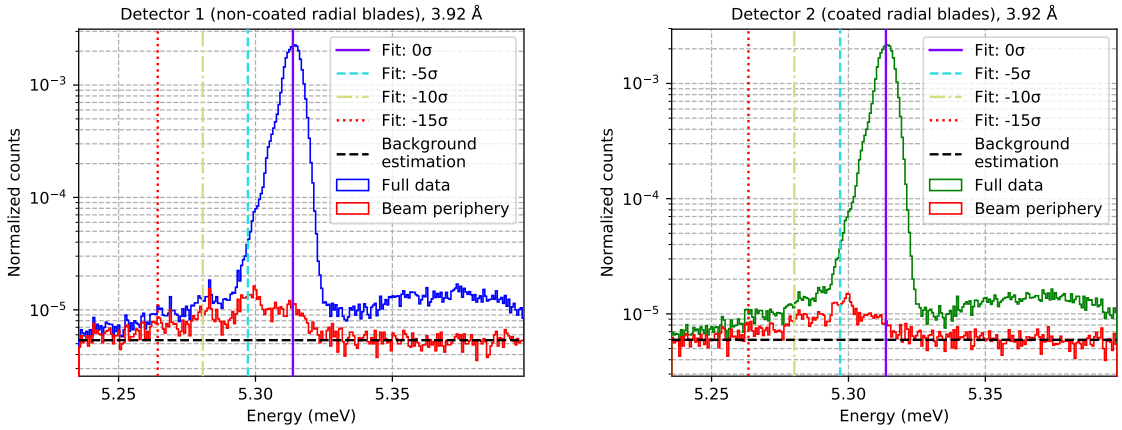

Figure 44: Effect on peak shape by internally scattered neutrons. Histograms from the full data in Detector 1 (blue) and Detector 2 (green) are compared to data where the direct beam is removed (red). The background estimation is shown as a black horizontal line. The integration limits are presented as vertical lines, including 0σ (solid), -5σ (dashed), -10σ (dash-dotted), and -15σ (dotted). The parameter σ is the standard-deviation around the peak center, calculated using a Gaussian fit. The number of counts are normalized by beam monitor data.

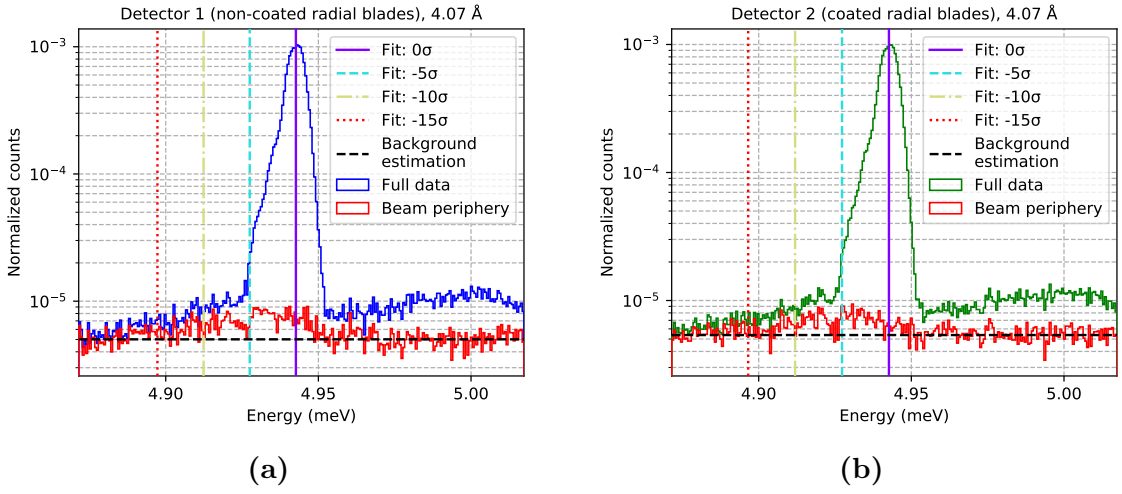

Figure 45: Effect on peak shape by internally scattered neutrons. Histograms from the full data in Detector 1 (blue) and Detector 2 (green) are compared to data where the direct beam is removed (red). The background estimation is shown as a black horizontal line. The integration limits are presented as vertical lines, including 0σ (solid), -5σ (dashed), -10σ (dash-dotted), and -15σ (dotted). The parameter σ is the standard-deviation around the peak center, calculated using a Gaussian fit. The number of counts are normalized by beam monitor data.

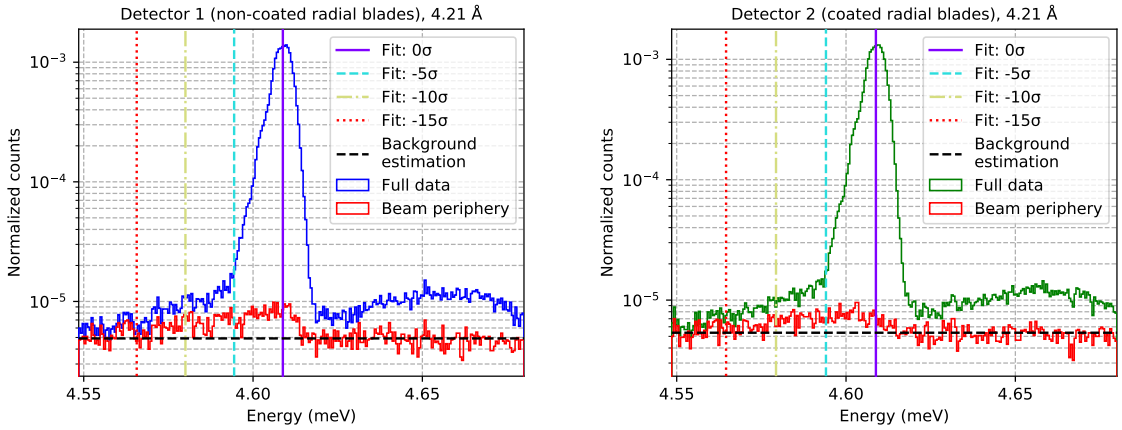

Figure 46: Effect on peak shape by internally scattered neutrons. Histograms from the full data in Detector 1 (blue) and Detector 2 (green) are compared to data where the direct beam is removed (red). The background estimation is shown as a black horizontal line. The integration limits are presented as vertical lines, including 0σ (solid), -5σ (dashed), -10σ (dash-dotted), and -15σ (dotted). The parameter σ is the standard-deviation around the peak center, calculated using a Gaussian fit. The number of counts are normalized by beam monitor data.

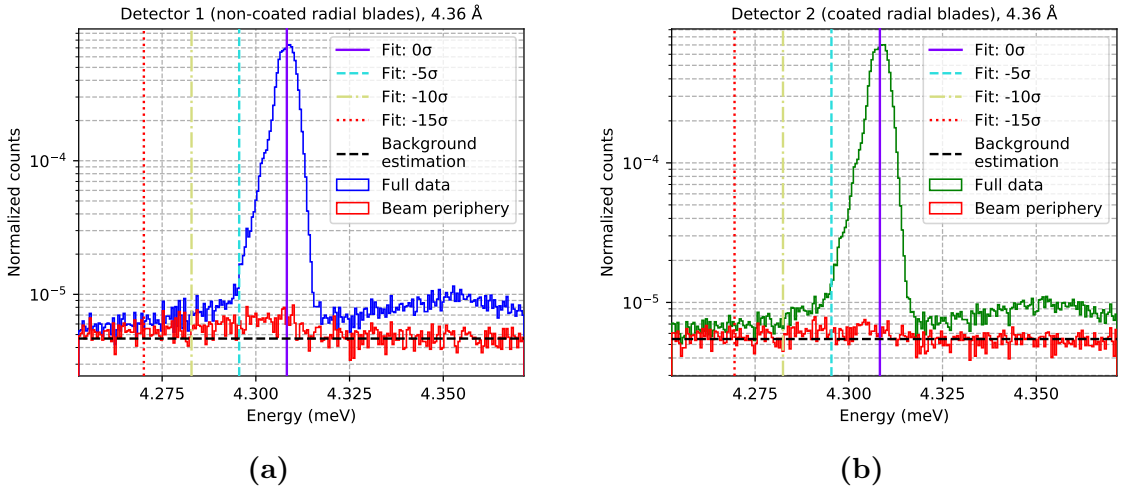

Figure 47: Effect on peak shape by internally scattered neutrons. Histograms from the full data in Detector 1 (blue) and Detector 2 (green) are compared to data where the direct beam is removed (red). The background estimation is shown as a black horizontal line. The integration limits are presented as vertical lines, including 0σ (solid), -5σ (dashed), -10σ (dash-dotted), and -15σ (dotted). The parameter σ is the standard-deviation around the peak center, calculated using a Gaussian fit. The number of counts are normalized by beam monitor data.

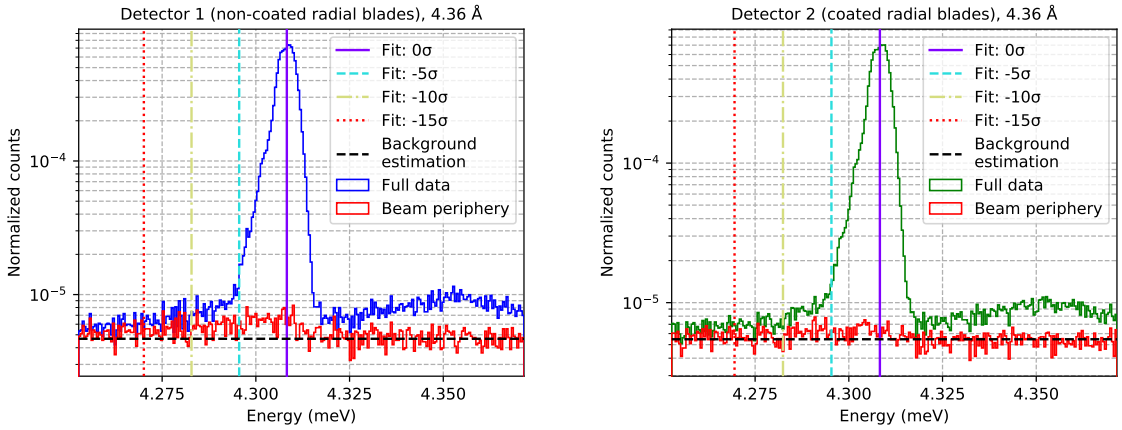

Figure 48: Effect on peak shape by internally scattered neutrons. Histograms from the full data in Detector 1 (blue) and Detector 2 (green) are compared to data where the direct beam is removed (red). The background estimation is shown as a black horizontal line. The integration limits are presented as vertical lines, including 0σ (solid), -5σ (dashed), -10σ (dash-dotted), and -15σ (dotted). The parameter σ is the standard-deviation around the peak center, calculated using a Gaussian fit. The number of counts are normalized by beam monitor data.

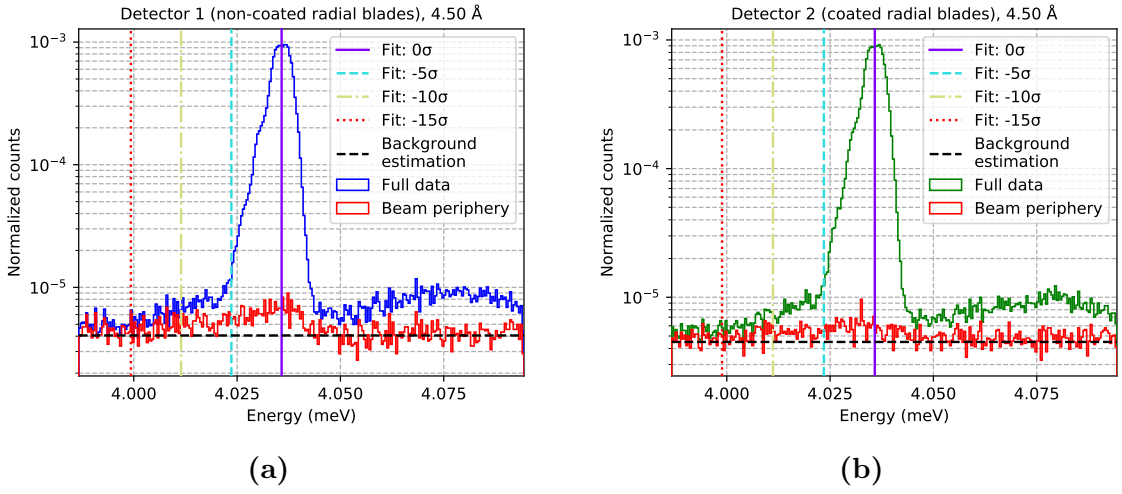

Figure 49: Effect on peak shape by internally scattered neutrons. Histograms from the full data in Detector 1 (blue) and Detector 2 (green) are compared to data where the direct beam is removed (red). The background estimation is shown as a black horizontal line. The integration limits are presented as vertical lines, including 0σ (solid), -5σ (dashed), -10σ (dash-dotted), and -15σ (dotted). The parameter σ is the standard-deviation around the peak center, calculated using a Gaussian fit. The number of counts are normalized by beam monitor data.

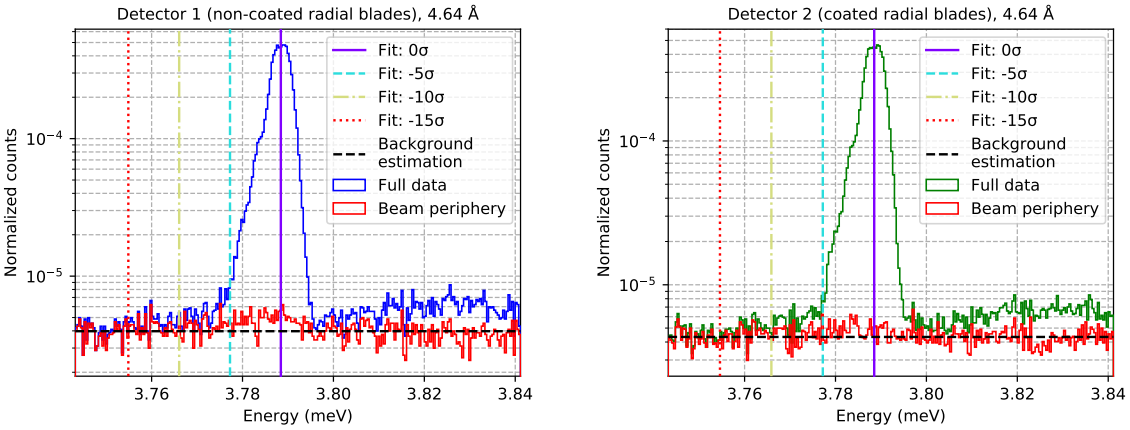

(a) **(b)**

Figure 50: Effect on peak shape by internally scattered neutrons. Histograms from the full data in Detector 1 (blue) and Detector 2 (green) are compared to data where the direct beam is removed (red). The background estimation is shown as a black horizontal line. The integration limits are presented as vertical lines, including 0σ (solid), -5σ (dashed), -10σ (dash-dotted), and -15σ (dotted). The parameter σ is the standard-deviation around the peak center, calculated using a Gaussian fit. The number of counts are normalized by beam monitor data.

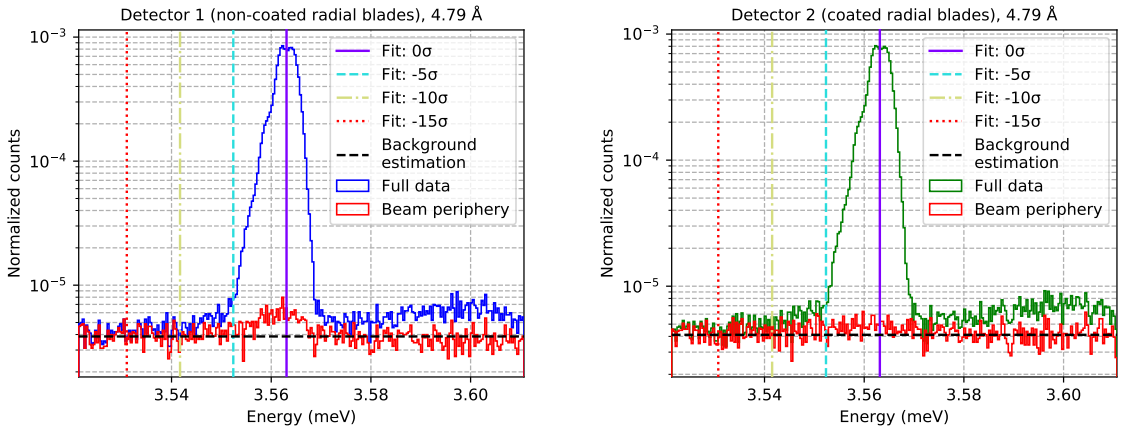

(a) **(b)**

Figure 51: Effect on peak shape by internally scattered neutrons. Histograms from the full data in Detector 1 (blue) and Detector 2 (green) are compared to data where the direct beam is removed (red). The background estimation is shown as a black horizontal line. The integration limits are presented as vertical lines, including 0σ (solid), -5σ (dashed), -10σ (dash-dotted), and -15σ (dotted). The parameter σ is the standard-deviation around the peak center, calculated using a Gaussian fit. The number of counts are normalized by beam monitor data.

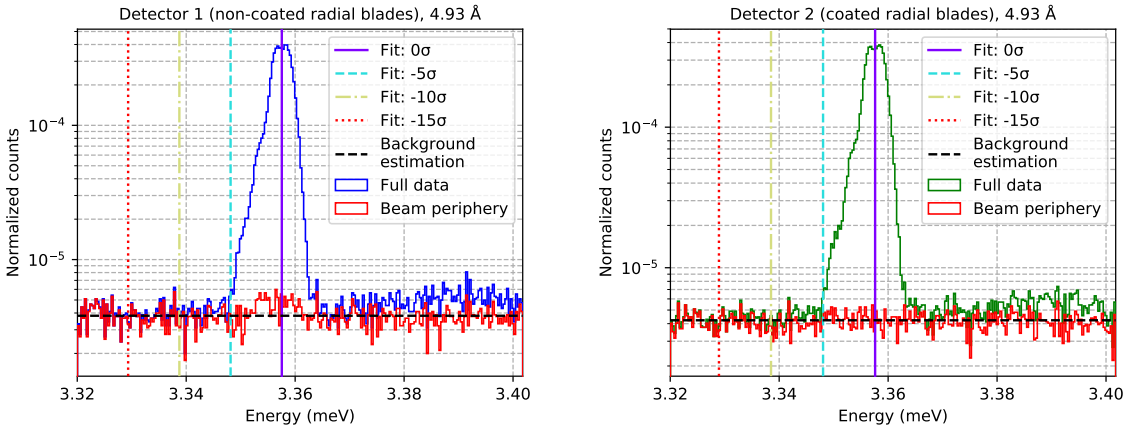

(a) **(b)**

Figure 52: Effect on peak shape by internally scattered neutrons. Histograms from the full data in Detector 1 (blue) and Detector 2 (green) are compared to data where the direct beam is removed (red). The background estimation is shown as a black horizontal line. The integration limits are presented as vertical lines, including 0σ (solid), -5σ (dashed), -10σ (dash-dotted), and -15σ (dotted). The parameter σ is the standard-deviation around the peak center, calculated using a Gaussian fit. The number of counts are normalized by beam monitor data.

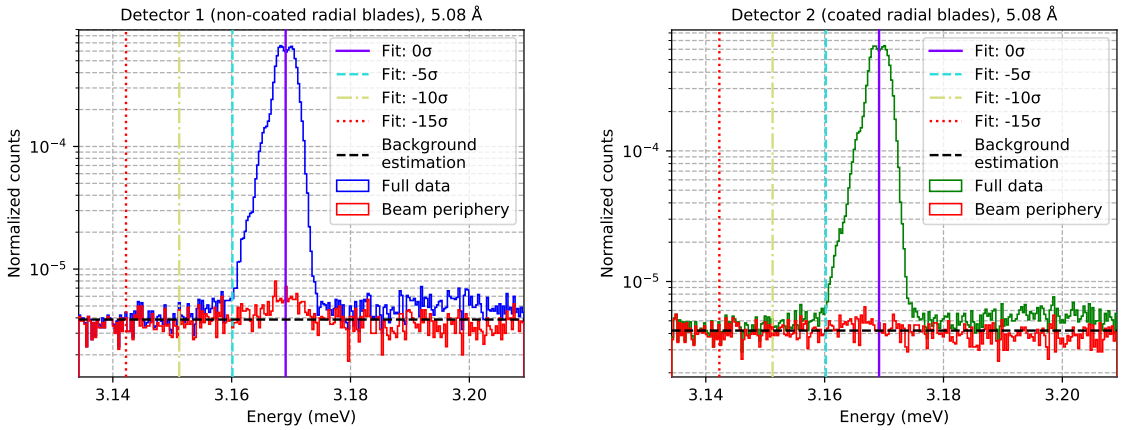

(a) **(b)**

Figure 53: Effect on peak shape by internally scattered neutrons. Histograms from the full data in Detector 1 (blue) and Detector 2 (green) are compared to data where the direct beam is removed (red). The background estimation is shown as a black horizontal line. The integration limits are presented as vertical lines, including 0σ (solid), -5σ (dashed), -10σ (dash-dotted), and -15σ (dotted). The parameter σ is the standard-deviation around the peak center, calculated using a Gaussian fit. The number of counts are normalized by beam monitor data.

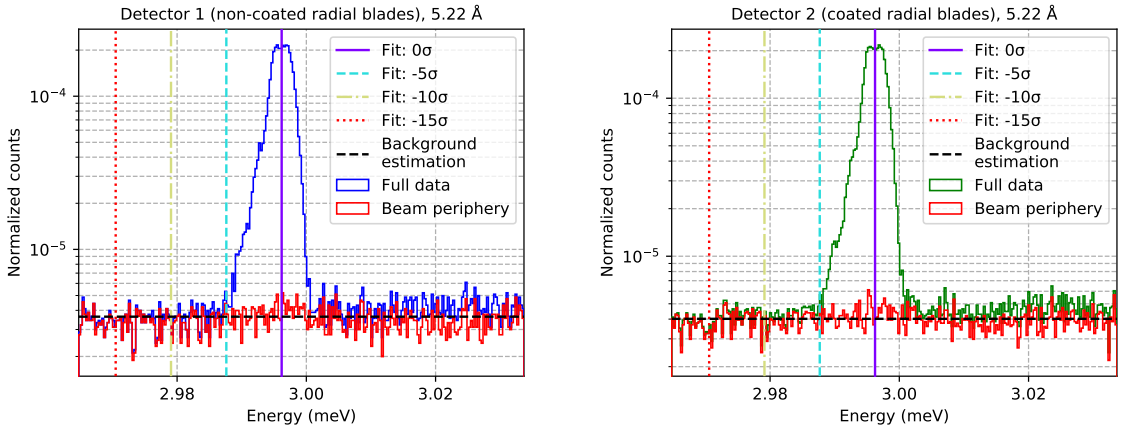

Figure 54: Effect on peak shape by internally scattered neutrons. Histograms from the full data in Detector 1 (blue) and Detector 2 (green) are compared to data where the direct beam is removed (red). The background estimation is shown as a black horizontal line. The integration limits are presented as vertical lines, including 0σ (solid), -5σ (dashed), -10σ (dash-dotted), and -15σ (dotted). The parameter σ is the standard-deviation around the peak center, calculated using a Gaussian fit. The number of counts are normalized by beam monitor data.

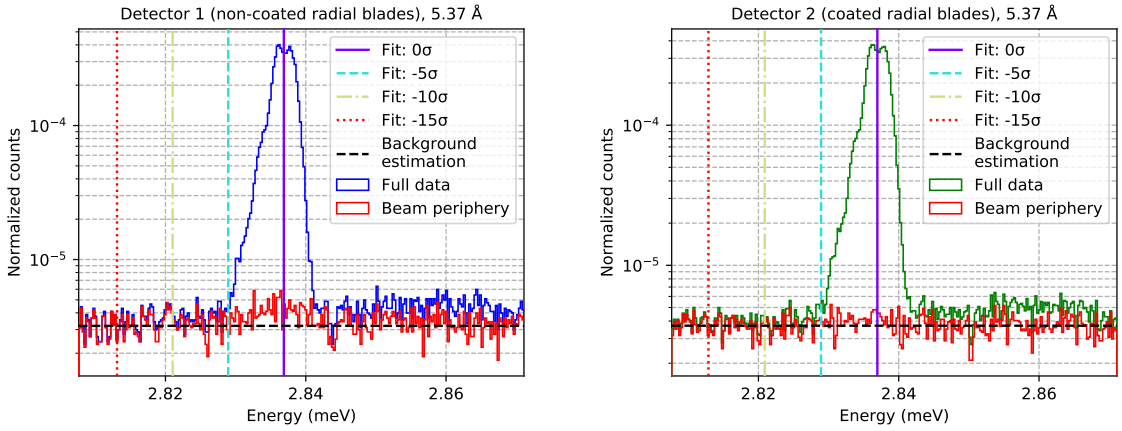

Figure 55: Effect on peak shape by internally scattered neutrons. Histograms from the full data in Detector 1 (blue) and Detector 2 (green) are compared to data where the direct beam is removed (red). The background estimation is shown as a black horizontal line. The integration limits are presented as vertical lines, including 0σ (solid), -5σ (dashed), -10σ (dash-dotted), and -15σ (dotted). The parameter σ is the standard-deviation around the peak center, calculated using a Gaussian fit. The number of counts are normalized by beam monitor data.

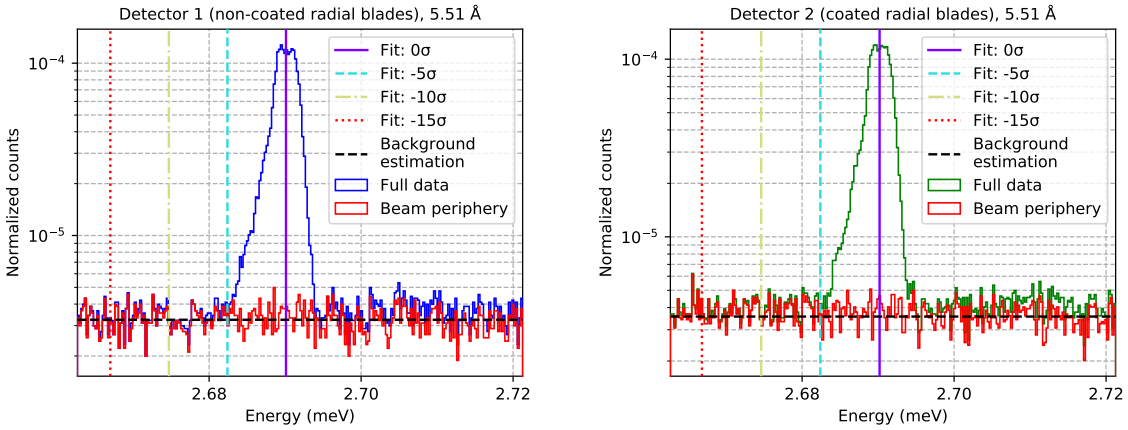

Figure 56: Effect on peak shape by internally scattered neutrons. Histograms from the full data in Detector 1 (blue) and Detector 2 (green) are compared to data where the direct beam is removed (red). The background estimation is shown as a black horizontal line. The integration limits are presented as vertical lines, including 0σ (solid), -5σ (dashed), -10σ (dash-dotted), and -15σ (dotted). The parameter σ is the standard-deviation around the peak center, calculated using a Gaussian fit. The number of counts are normalized by beam monitor data.

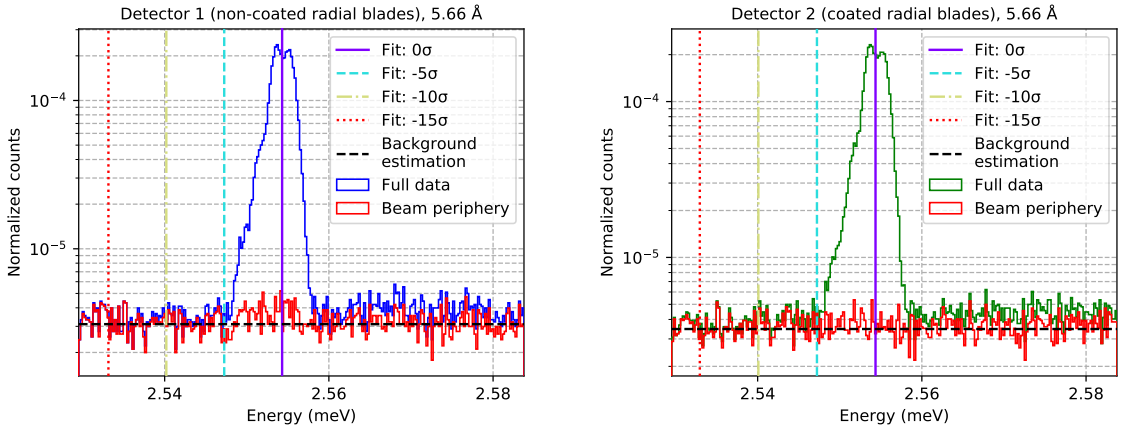

Figure 57: Effect on peak shape by internally scattered neutrons. Histograms from the full data in Detector 1 (blue) and Detector 2 (green) are compared to data where the direct beam is removed (red). The background estimation is shown as a black horizontal line. The integration limits are presented as vertical lines, including 0σ (solid), -5σ (dashed), -10σ (dash-dotted), and -15σ (dotted). The parameter σ is the standard-deviation around the peak center, calculated using a Gaussian fit. The number of counts are normalized by beam monitor data.

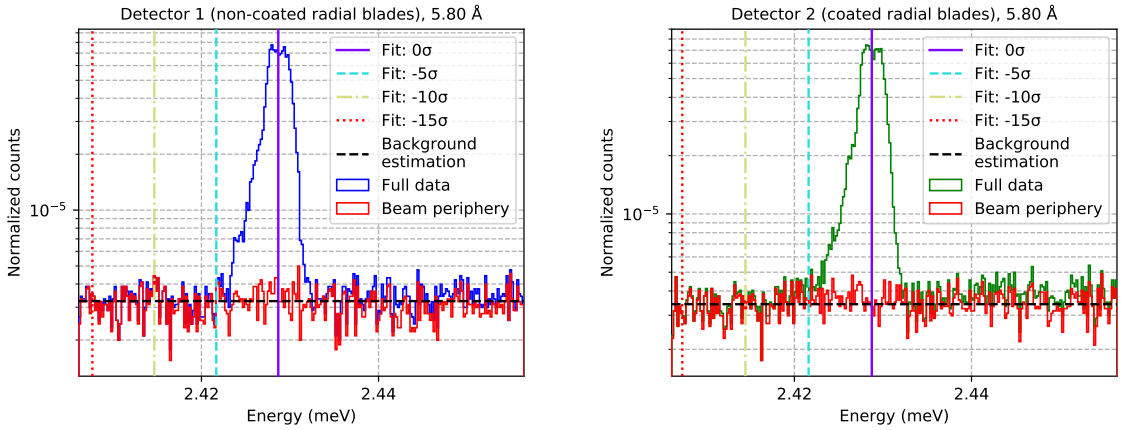

(a) **(b)**

Figure 58: Effect on peak shape by internally scattered neutrons. Histograms from the full data in Detector 1 (blue) and Detector 2 (green) are compared to data where the direct beam is removed (red). The background estimation is shown as a black horizontal line. The integration limits are presented as vertical lines, including 0σ (solid), -5σ (dashed), -10σ (dash-dotted), and -15σ (dotted). The parameter σ is the standard-deviation around the peak center, calculated using a Gaussian fit. The number of counts are normalized by beam monitor data.

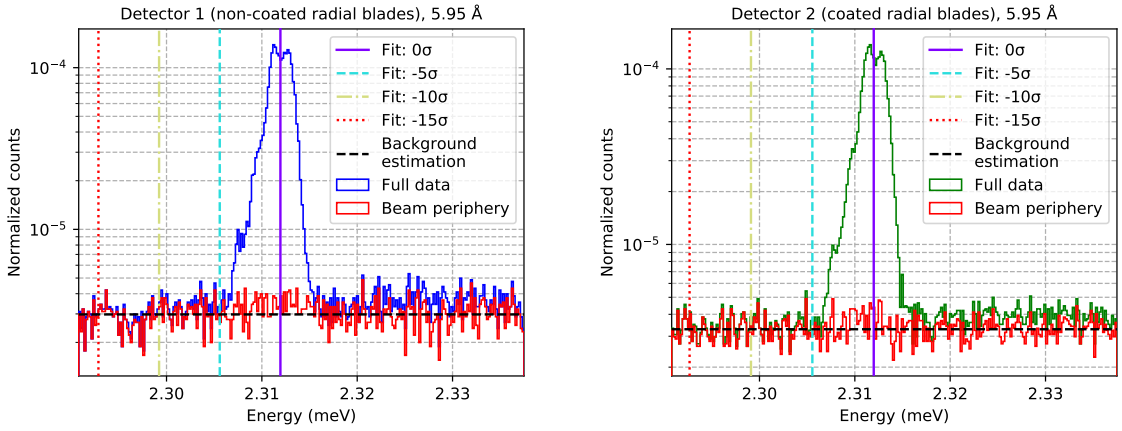

(a) **(b)**

Figure 59: Effect on peak shape by internally scattered neutrons. Histograms from the full data in Detector 1 (blue) and Detector 2 (green) are compared to data where the direct beam is removed (red). The background estimation is shown as a black horizontal line. The integration limits are presented as vertical lines, including 0σ (solid), -5σ (dashed), -10σ (dash-dotted), and -15σ (dotted). The parameter σ is the standard-deviation around the peak center, calculated using a Gaussian fit. The number of counts are normalized by beam monitor data.

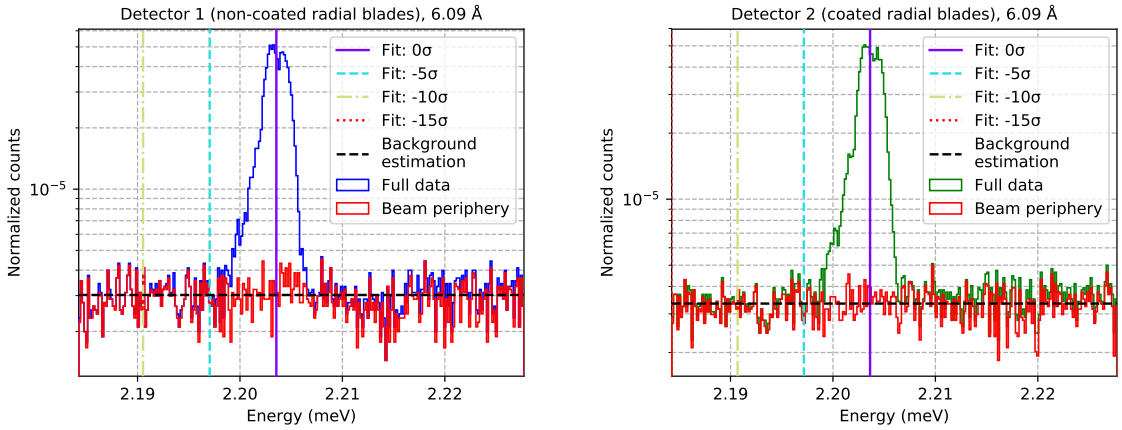

(a) **(b)**

Figure 60: Effect on peak shape by internally scattered neutrons. Histograms from the full data in Detector 1 (blue) and Detector 2 (green) are compared to data where the direct beam is removed (red). The background estimation is shown as a black horizontal line. The integration limits are presented as vertical lines, including 0σ (solid), -5σ (dashed), -10σ (dash-dotted), and -15σ (dotted). The parameter σ is the standard-deviation around the peak center, calculated using a Gaussian fit. The number of counts are normalized by beam monitor data.

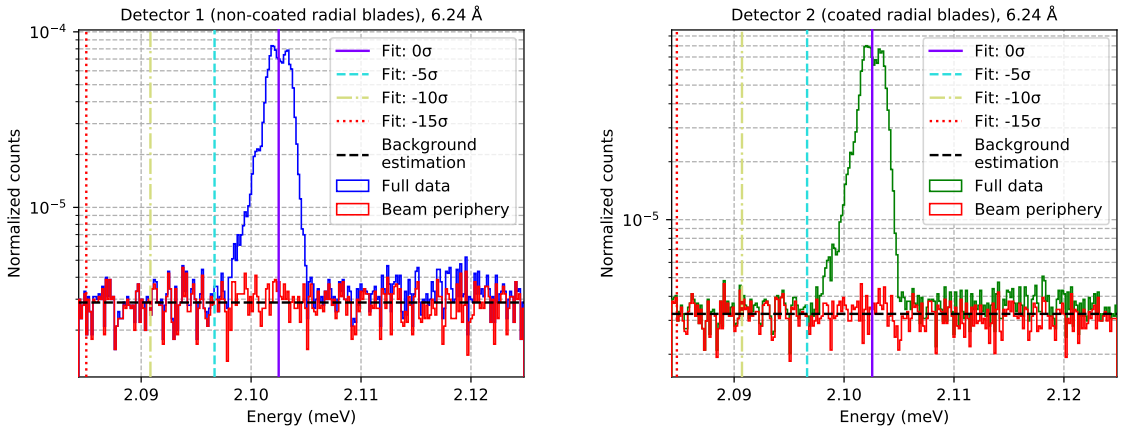

(a) **(b)**

Figure 61: Effect on peak shape by internally scattered neutrons. Histograms from the full data in Detector 1 (blue) and Detector 2 (green) are compared to data where the direct beam is removed (red). The background estimation is shown as a black horizontal line. The integration limits are presented as vertical lines, including 0σ (solid), -5σ (dashed), -10σ (dash-dotted), and -15σ (dotted). The parameter σ is the standard-deviation around the peak center, calculated using a Gaussian fit. The number of counts are normalized by beam monitor data.

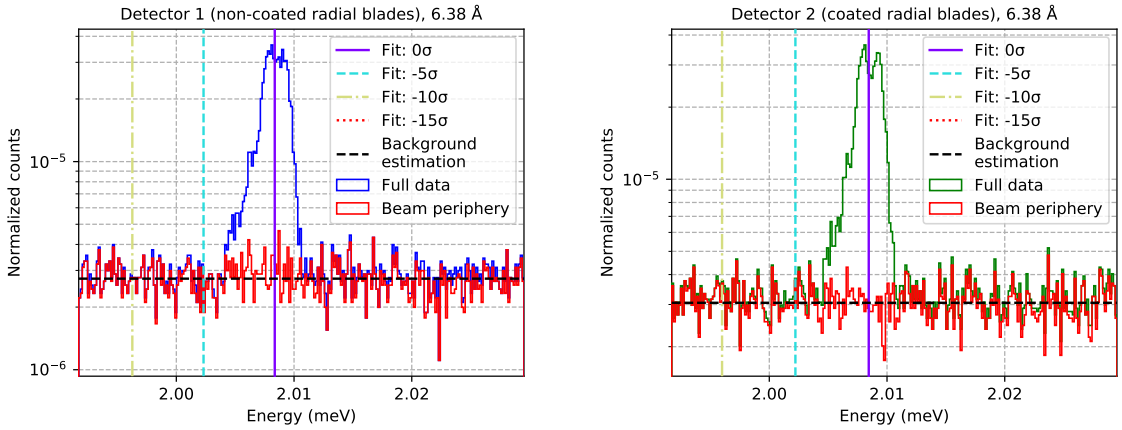

Figure 62: Effect on peak shape by internally scattered neutrons. Histograms from the full data in Detector 1 (blue) and Detector 2 (green) are compared to data where the direct beam is removed (red). The background estimation is shown as a black horizontal line. The integration limits are presented as vertical lines, including 0σ (solid), -5σ (dashed), -10σ (dash-dotted), and -15σ (dotted). The parameter σ is the standard-deviation around the peak center, calculated using a Gaussian fit. The number of counts are normalized by beam monitor data.

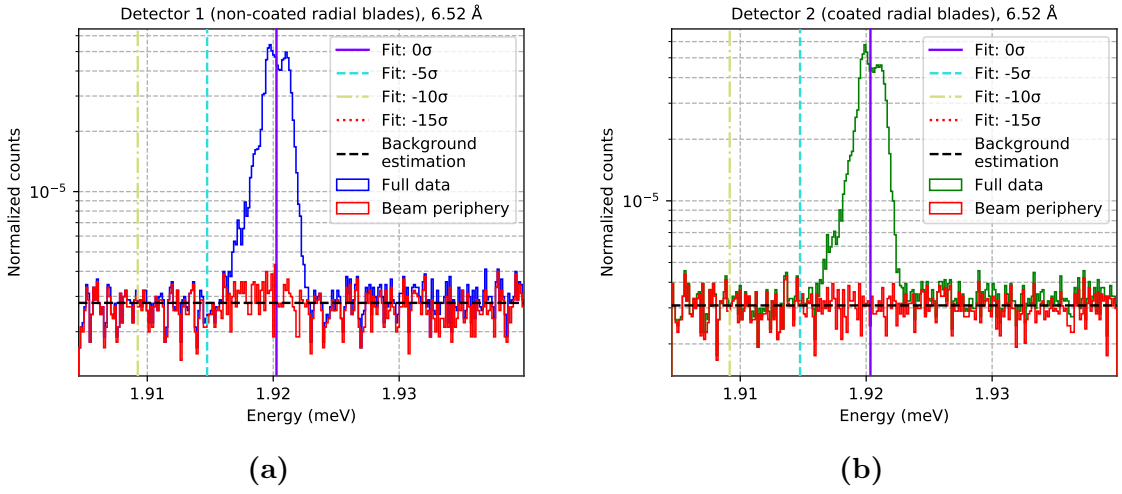

Figure 63: Effect on peak shape by internally scattered neutrons. Histograms from the full data in Detector 1 (blue) and Detector 2 (green) are compared to data where the direct beam is removed (red). The background estimation is shown as a black horizontal line. The integration limits are presented as vertical lines, including 0σ (solid), -5σ (dashed), -10σ (dash-dotted), and -15σ (dotted). The parameter σ is the standard-deviation around the peak center, calculated using a Gaussian fit. The number of counts are normalized by beam monitor data.

3. Energy resolution

In figure 64 to 86, the pulse width correction analysis for the Multi-Grid detector is presented. In each figure, a separate peak is studied, ranging from approximately 1.5 to 4.5 Å. The wavelength corresponding to the peak center is stated in each figure title. The Gaussian fittings of the energy peaks from each Multi-Grid layer are presented (left), together with the interpolation of the acquired FWHM values from each layer (right). In the right plots, the FWHM of the helium-3 tube is presented in red.

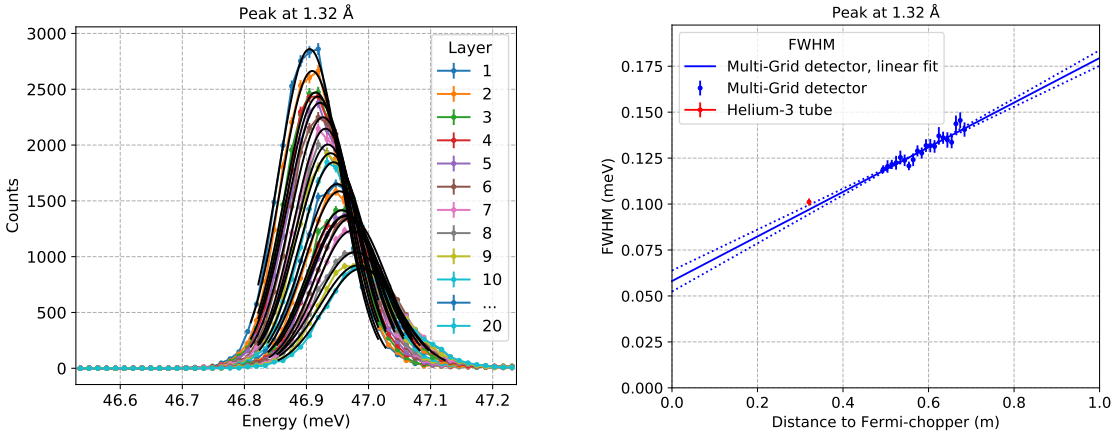

(a) **(b)**

Figure 64: At the left, the widening in energy is presented for each layer. The neutron energy distributions from each layer is fitted with a Gaussian (black) and the FWHM is extracted from the fit parameters. At the right, the FWHM from each Multi-Grid layer (blue) is shown together with the FWHM of the helium-3 tube (red), as a function of the distance from the Fermi-chopper. A linear fit (blue line) from the Multi-Grid points is also presented, demonstrating how the chopper pulse widens with distance. The fit uncertainties are presented as dashed lines.

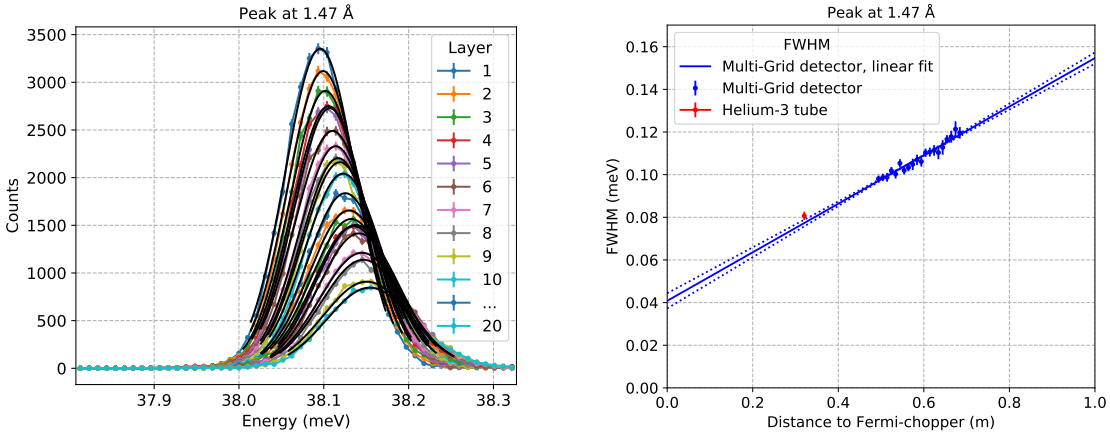

(a) **(b)**

Figure 65: At the left, the widening in energy is presented for each layer. The neutron energy distributions from each layer is fitted with a Gaussian (black) and the FWHM is extracted from the fit parameters. At the right, the FWHM from each Multi-Grid layer (blue) is shown together with the FWHM of the helium-3 tube (red), as a function of the distance from the Fermi-chopper. A linear fit (blue line) from the Multi-Grid points is also presented, demonstrating how the chopper pulse widens with distance. The fit uncertainties are presented as dashed lines.

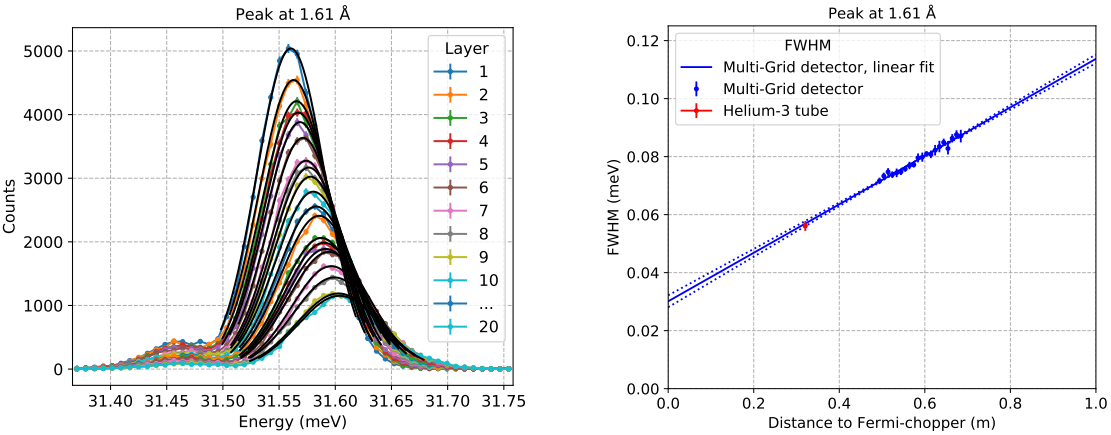

(a) **(b)**

Figure 66: At the left, the widening in energy is presented for each layer. The neutron energy distributions from each layer is fitted with a Gaussian (black) and the FWHM is extracted from the fit parameters. At the right, the FWHM from each Multi-Grid layer (blue) is shown together with the FWHM of the helium-3 tube (red), as a function of the distance from the Fermi-chopper. A linear fit (blue line) from the Multi-Grid points is also presented, demonstrating how the chopper pulse widens with distance. The fit uncertainties are presented as dashed lines.

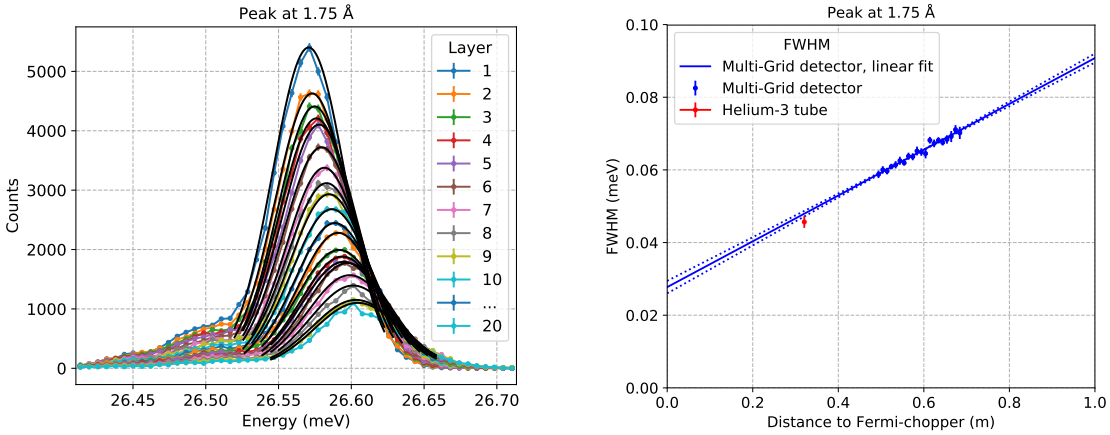

(a) **(b)**

Figure 67: At the left, the widening in energy is presented for each layer. The neutron energy distributions from each layer is fitted with a Gaussian (black) and the FWHM is extracted from the fit parameters. At the right, the FWHM from each Multi-Grid layer (blue) is shown together with the FWHM of the helium-3 tube (red), as a function of the distance from the Fermi-chopper. A linear fit (blue line) from the Multi-Grid points is also presented, demonstrating how the chopper pulse widens with distance. The fit uncertainties are presented as dashed lines.

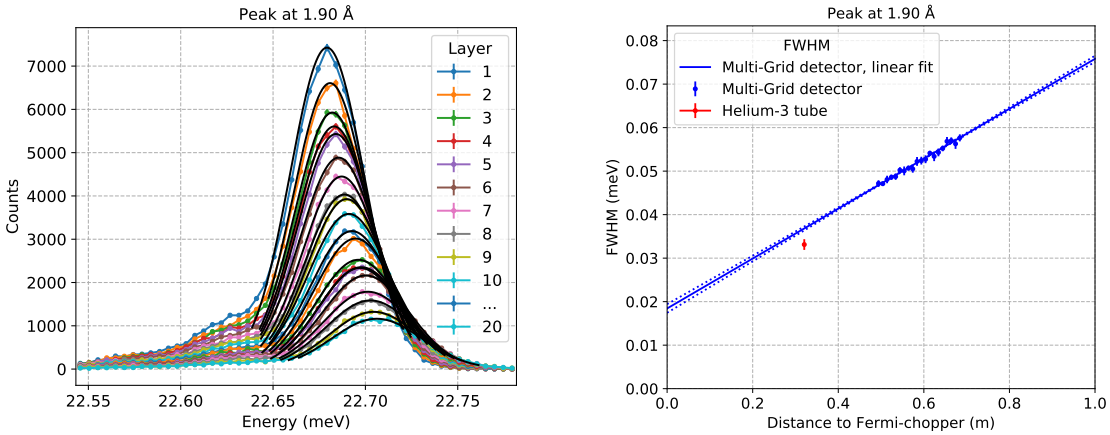

(a) **(b)**

Figure 68: At the left, the widening in energy is presented for each layer. The neutron energy distributions from each layer is fitted with a Gaussian (black) and the FWHM is extracted from the fit parameters. At the right, the FWHM from each Multi-Grid layer (blue) is shown together with the FWHM of the helium-3 tube (red), as a function of the distance from the Fermi-chopper. A linear fit (blue line) from the Multi-Grid points is also presented, demonstrating how the chopper pulse widens with distance. The fit uncertainties are presented as dashed lines.

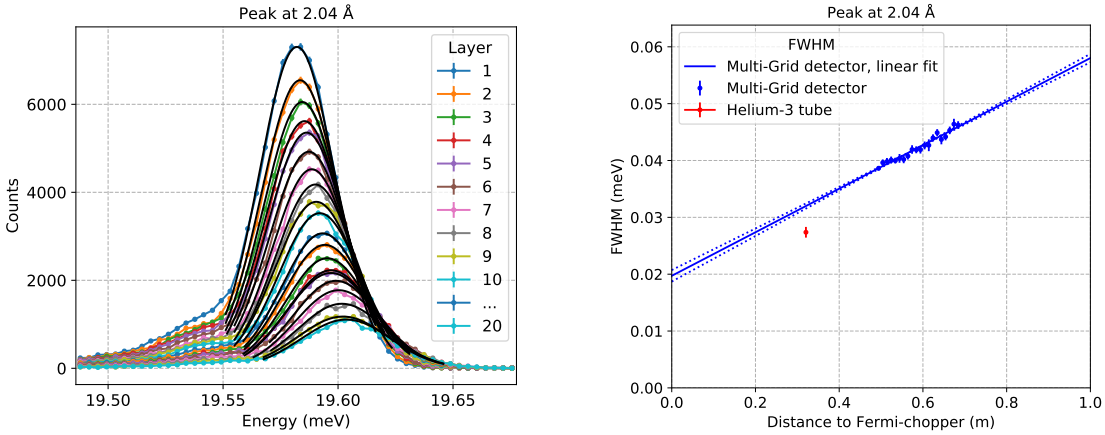

(a) **(b)**

Figure 69: At the left, the widening in energy is presented for each layer. The neutron energy distributions from each layer is fitted with a Gaussian (black) and the FWHM is extracted from the fit parameters. At the right, the FWHM from each Multi-Grid layer (blue) is shown together with the FWHM of the helium-3 tube (red), as a function of the distance from the Fermi-chopper. A linear fit (blue line) from the Multi-Grid points is also presented, demonstrating how the chopper pulse widens with distance. The fit uncertainties are presented as dashed lines.

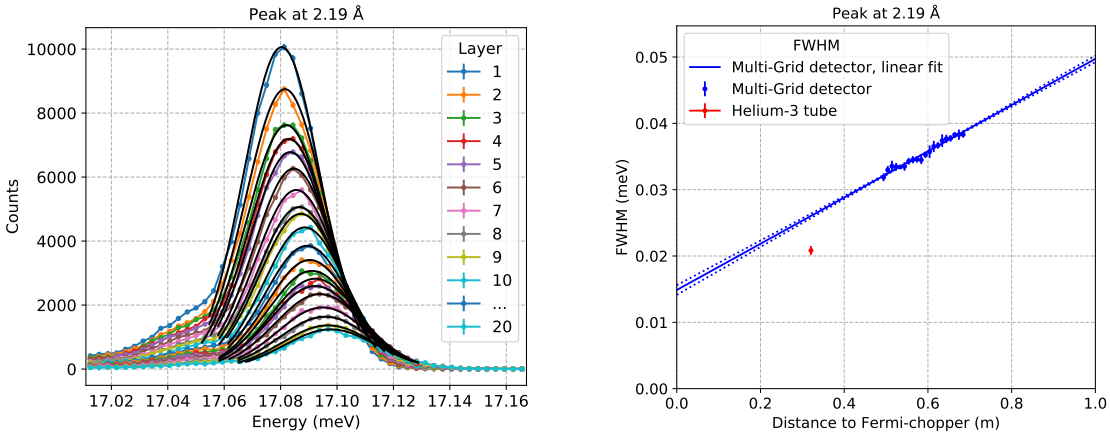

(a) **(b)**

Figure 70: At the left, the widening in energy is presented for each layer. The neutron energy distributions from each layer is fitted with a Gaussian (black) and the FWHM is extracted from the fit parameters. At the right, the FWHM from each Multi-Grid layer (blue) is shown together with the FWHM of the helium-3 tube (red), as a function of the distance from the Fermi-chopper. A linear fit (blue line) from the Multi-Grid points is also presented, demonstrating how the chopper pulse widens with distance. The fit uncertainties are presented as dashed lines.

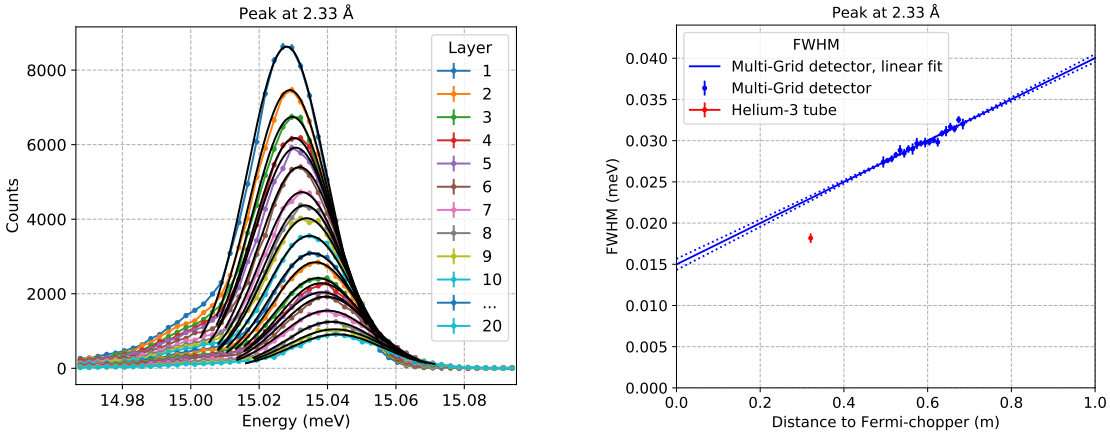

(a) **(b)**

Figure 71: At the left, the widening in energy is presented for each layer. The neutron energy distributions from each layer is fitted with a Gaussian (black) and the FWHM is extracted from the fit parameters. At the right, the FWHM from each Multi-Grid layer (blue) is shown together with the FWHM of the helium-3 tube (red), as a function of the distance from the Fermi-chopper. A linear fit (blue line) from the Multi-Grid points is also presented, demonstrating how the chopper pulse widens with distance. The fit uncertainties are presented as dashed lines.

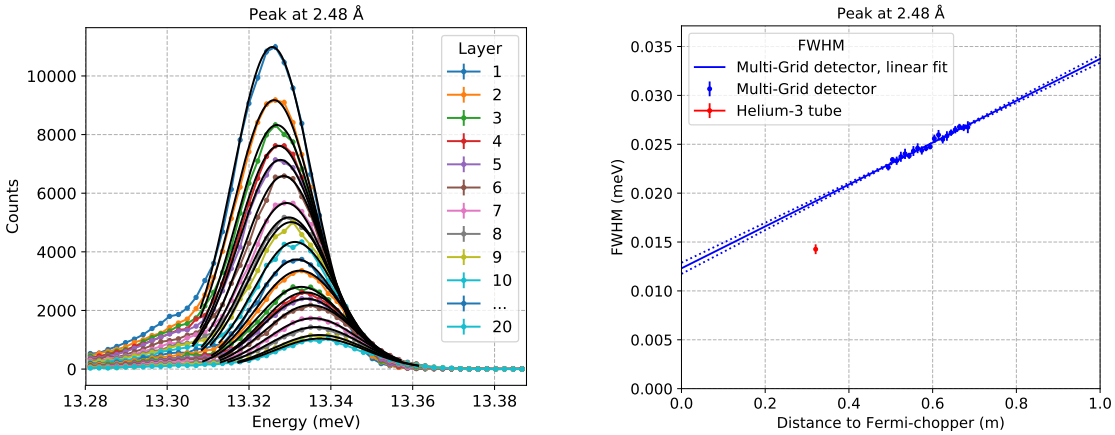

(a) **(b)**

Figure 72: At the left, the widening in energy is presented for each layer. The neutron energy distributions from each layer is fitted with a Gaussian (black) and the FWHM is extracted from the fit parameters. At the right, the FWHM from each Multi-Grid layer (blue) is shown together with the FWHM of the helium-3 tube (red), as a function of the distance from the Fermi-chopper. A linear fit (blue line) from the Multi-Grid points is also presented, demonstrating how the chopper pulse widens with distance. The fit uncertainties are presented as dashed lines.

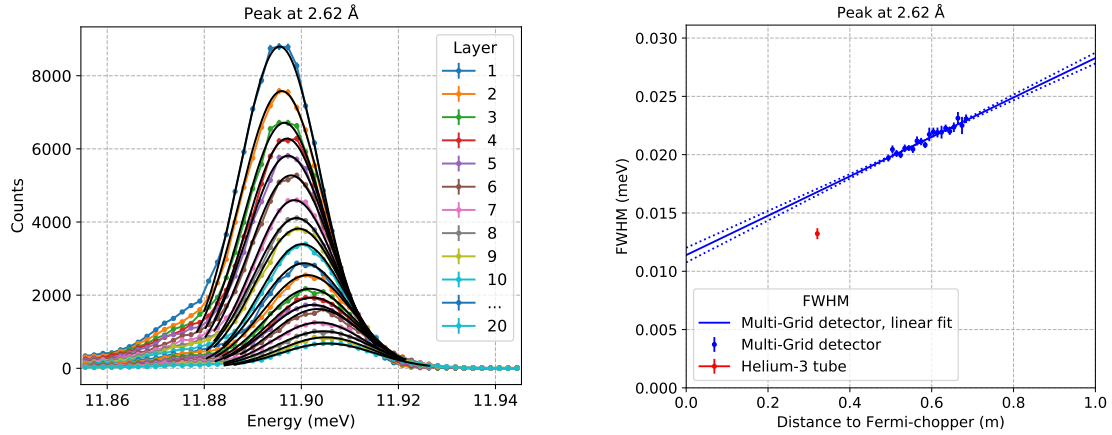

(a) **(b)**

Figure 73: At the left, the widening in energy is presented for each layer. The neutron energy distributions from each layer is fitted with a Gaussian (black) and the FWHM is extracted from the fit parameters. At the right, the FWHM from each Multi-Grid layer (blue) is shown together with the FWHM of the helium-3 tube (red), as a function of the distance from the Fermi-chopper. A linear fit (blue line) from the Multi-Grid points is also presented, demonstrating how the chopper pulse widens with distance. The fit uncertainties are presented as dashed lines.

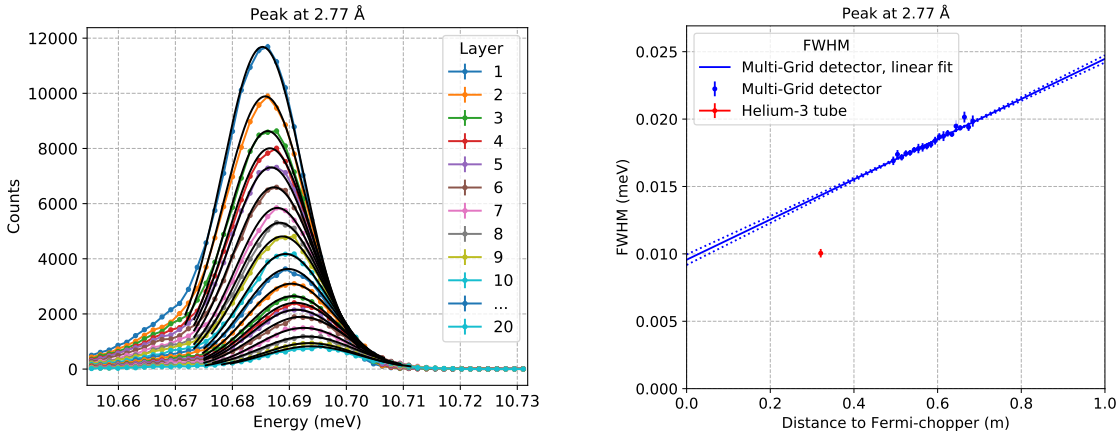

(a) **(b)**

Figure 74: At the left, the widening in energy is presented for each layer. The neutron energy distributions from each layer is fitted with a Gaussian (black) and the FWHM is extracted from the fit parameters. At the right, the FWHM from each Multi-Grid layer (blue) is shown together with the FWHM of the helium-3 tube (red), as a function of the distance from the Fermi-chopper. A linear fit (blue line) from the Multi-Grid points is also presented, demonstrating how the chopper pulse widens with distance. The fit uncertainties are presented as dashed lines.

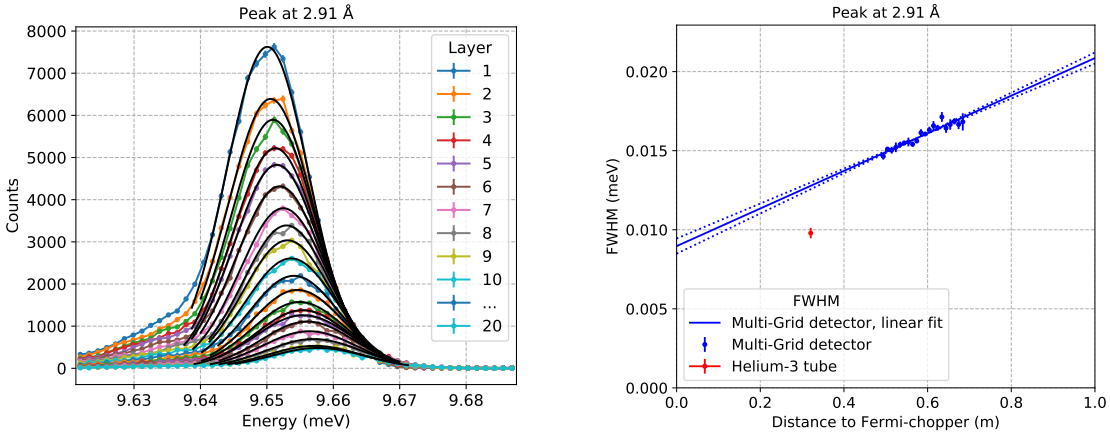

(a) **(b)**

Figure 75: At the left, the widening in energy is presented for each layer. The neutron energy distributions from each layer is fitted with a Gaussian (black) and the FWHM is extracted from the fit parameters. At the right, the FWHM from each Multi-Grid layer (blue) is shown together with the FWHM of the helium-3 tube (red), as a function of the distance from the Fermi-chopper. A linear fit (blue line) from the Multi-Grid points is also presented, demonstrating how the chopper pulse widens with distance. The fit uncertainties are presented as dashed lines.

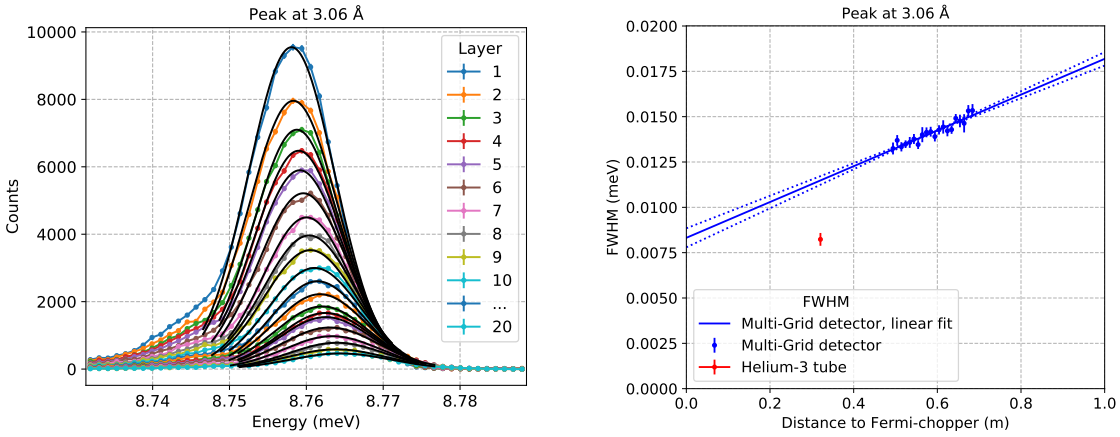

(a) **(b)**

Figure 76: At the left, the widening in energy is presented for each layer. The neutron energy distributions from each layer is fitted with a Gaussian (black) and the FWHM is extracted from the fit parameters. At the right, the FWHM from each Multi-Grid layer (blue) is shown together with the FWHM of the helium-3 tube (red), as a function of the distance from the Fermi-chopper. A linear fit (blue line) from the Multi-Grid points is also presented, demonstrating how the chopper pulse widens with distance. The fit uncertainties are presented as dashed lines.

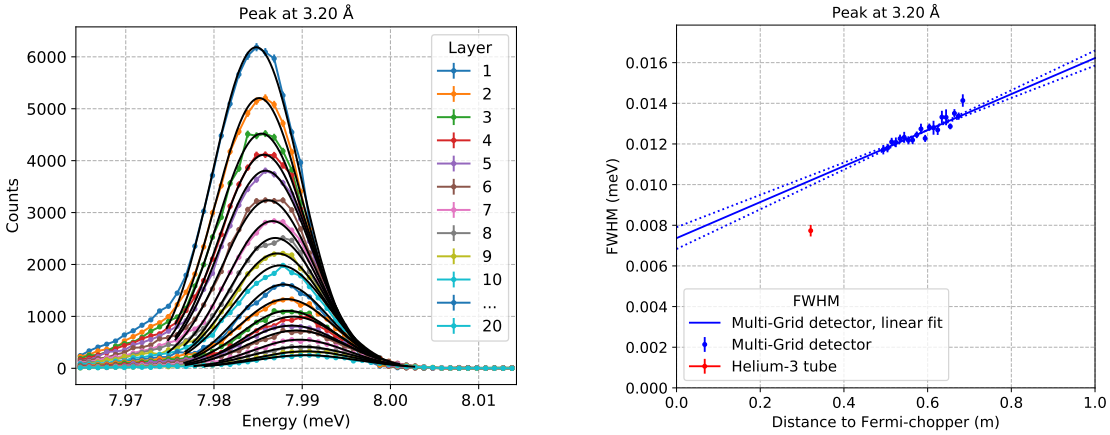

(a) **(b)**

Figure 77: At the left, the widening in energy is presented for each layer. The neutron energy distributions from each layer is fitted with a Gaussian (black) and the FWHM is extracted from the fit parameters. At the right, the FWHM from each Multi-Grid layer (blue) is shown together with the FWHM of the helium-3 tube (red), as a function of the distance from the Fermi-chopper. A linear fit (blue line) from the Multi-Grid points is also presented, demonstrating how the chopper pulse widens with distance. The fit uncertainties are presented as dashed lines.

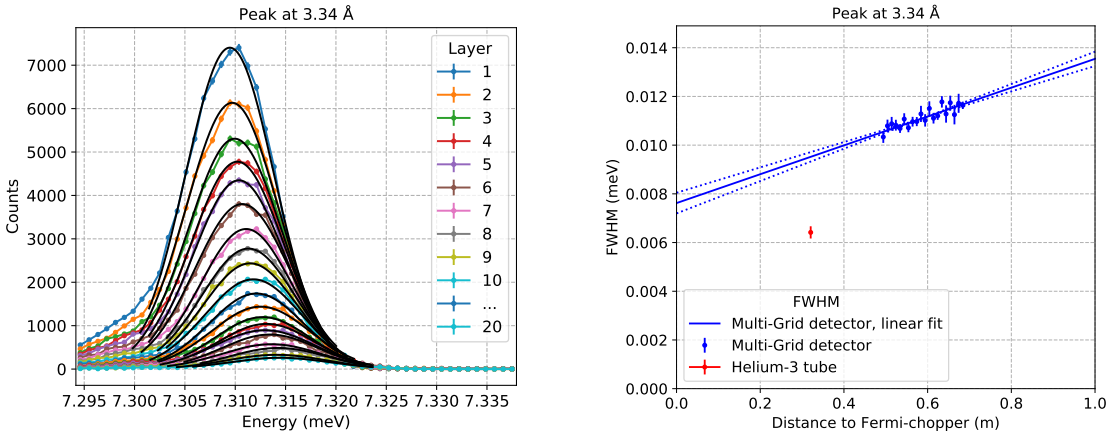

(a) **(b)**

Figure 78: At the left, the widening in energy is presented for each layer. The neutron energy distributions from each layer is fitted with a Gaussian (black) and the FWHM is extracted from the fit parameters. At the right, the FWHM from each Multi-Grid layer (blue) is shown together with the FWHM of the helium-3 tube (red), as a function of the distance from the Fermi-chopper. A linear fit (blue line) from the Multi-Grid points is also presented, demonstrating how the chopper pulse widens with distance. The fit uncertainties are presented as dashed lines.

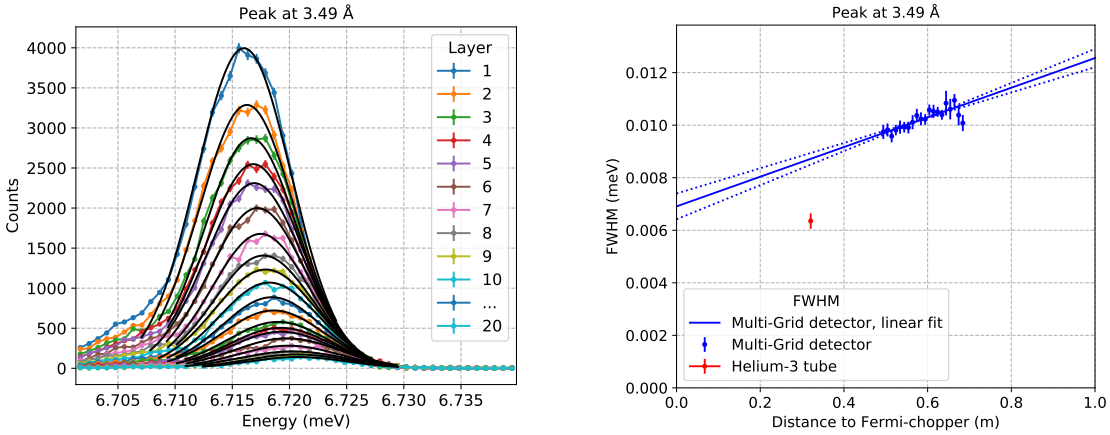

(a) **(b)**

Figure 79: At the left, the widening in energy is presented for each layer. The neutron energy distributions from each layer is fitted with a Gaussian (black) and the FWHM is extracted from the fit parameters. At the right, the FWHM from each Multi-Grid layer (blue) is shown together with the FWHM of the helium-3 tube (red), as a function of the distance from the Fermi-chopper. A linear fit (blue line) from the Multi-Grid points is also presented, demonstrating how the chopper pulse widens with distance. The fit uncertainties are presented as dashed lines.

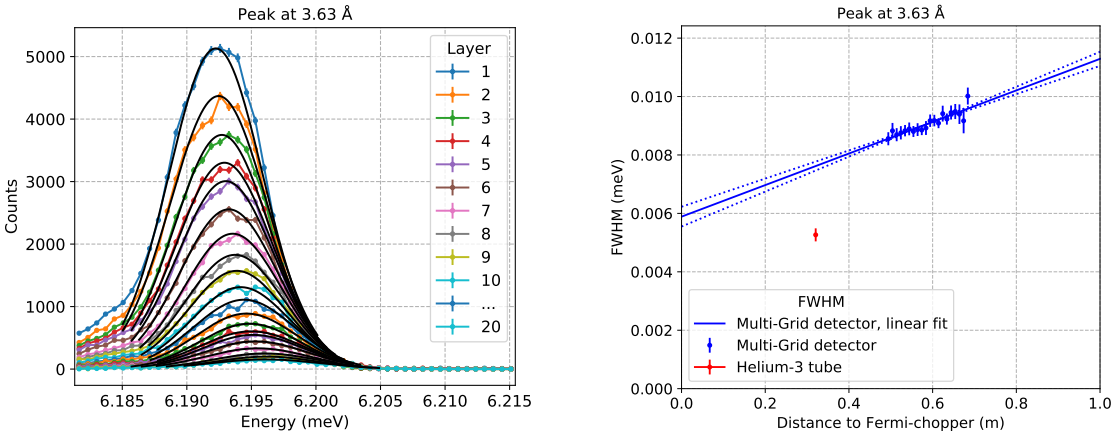

(a) **(b)**

Figure 80: At the left, the widening in energy is presented for each layer. The neutron energy distributions from each layer is fitted with a Gaussian (black) and the FWHM is extracted from the fit parameters. At the right, the FWHM from each Multi-Grid layer (blue) is shown together with the FWHM of the helium-3 tube (red), as a function of the distance from the Fermi-chopper. A linear fit (blue line) from the Multi-Grid points is also presented, demonstrating how the chopper pulse widens with distance. The fit uncertainties are presented as dashed lines.

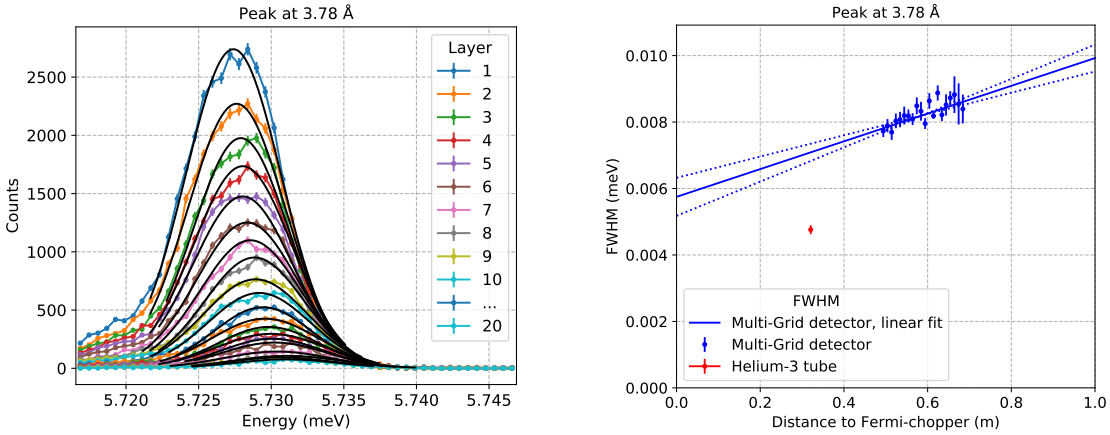

(a) **(b)**

Figure 81: At the left, the widening in energy is presented for each layer. The neutron energy distributions from each layer is fitted with a Gaussian (black) and the FWHM is extracted from the fit parameters. At the right, the FWHM from each Multi-Grid layer (blue) is shown together with the FWHM of the helium-3 tube (red), as a function of the distance from the Fermi-chopper. A linear fit (blue line) from the Multi-Grid points is also presented, demonstrating how the chopper pulse widens with distance. The fit uncertainties are presented as dashed lines.

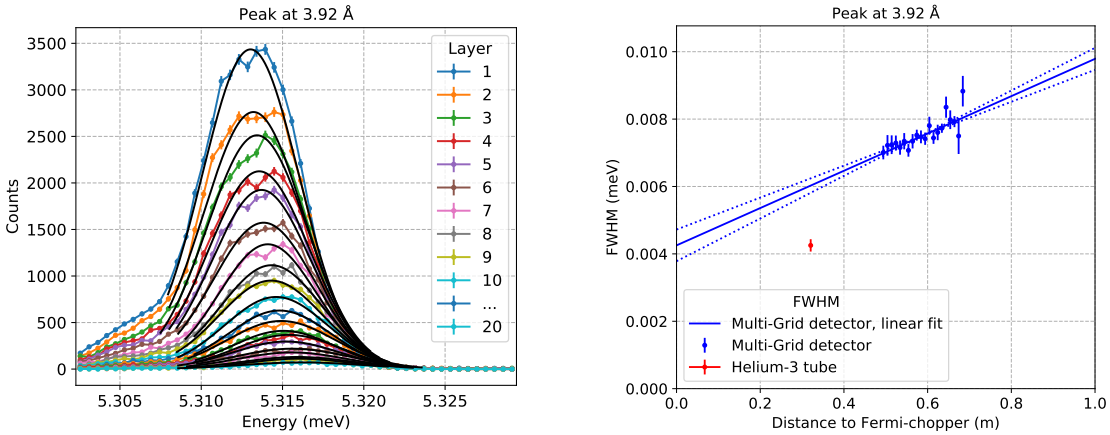

(a) **(b)**

Figure 82: At the left, the widening in energy is presented for each layer. The neutron energy distributions from each layer is fitted with a Gaussian (black) and the FWHM is extracted from the fit parameters. At the right, the FWHM from each Multi-Grid layer (blue) is shown together with the FWHM of the helium-3 tube (red), as a function of the distance from the Fermi-chopper. A linear fit (blue line) from the Multi-Grid points is also presented, demonstrating how the chopper pulse widens with distance. The fit uncertainties are presented as dashed lines.

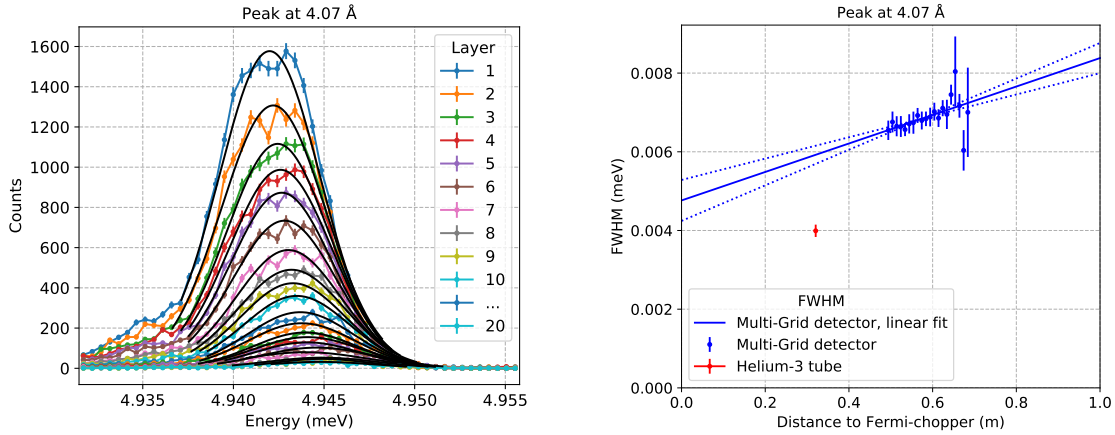

(a) **(b)**

Figure 83: At the left, the widening in energy is presented for each layer. The neutron energy distributions from each layer is fitted with a Gaussian (black) and the FWHM is extracted from the fit parameters. At the right, the FWHM from each Multi-Grid layer (blue) is shown together with the FWHM of the helium-3 tube (red), as a function of the distance from the Fermi-chopper. A linear fit (blue line) from the Multi-Grid points is also presented, demonstrating how the chopper pulse widens with distance. The fit uncertainties are presented as dashed lines.

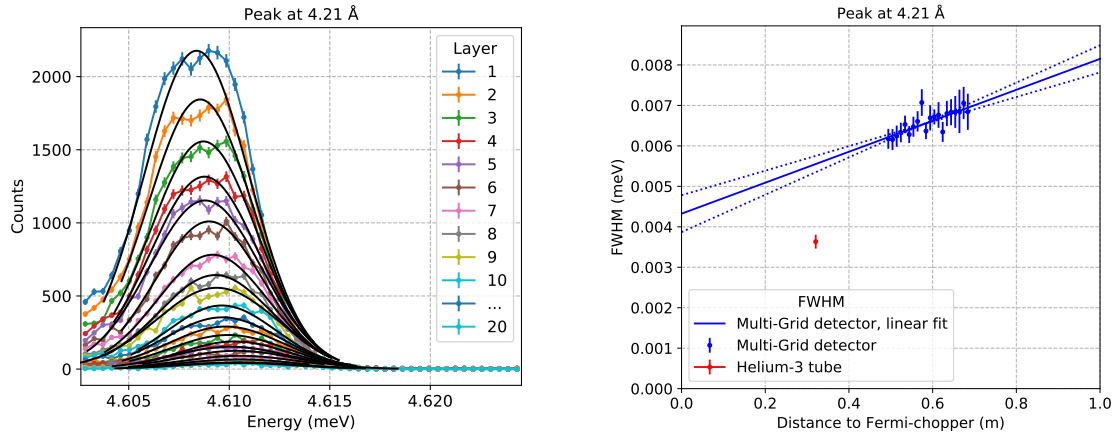

(a) **(b)**

Figure 84: At the left, the widening in energy is presented for each layer. The neutron energy distributions from each layer is fitted with a Gaussian (black) and the FWHM is extracted from the fit parameters. At the right, the FWHM from each Multi-Grid layer (blue) is shown together with the FWHM of the helium-3 tube (red), as a function of the distance from the Fermi-chopper. A linear fit (blue line) from the Multi-Grid points is also presented, demonstrating how the chopper pulse widens with distance. The fit uncertainties are presented as dashed lines.

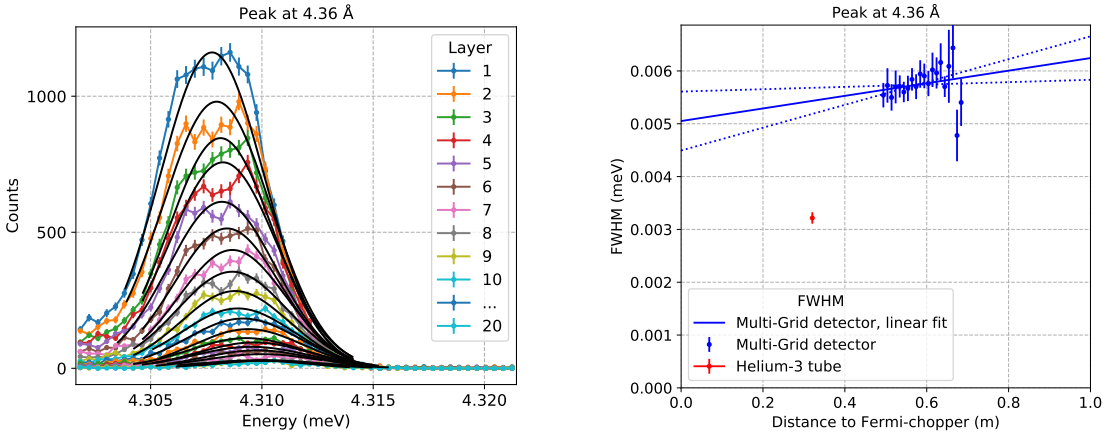

(a) **(b)**

Figure 85: At the left, the widening in energy is presented for each layer. The neutron energy distributions from each layer is fitted with a Gaussian (black) and the FWHM is extracted from the fit parameters. At the right, the FWHM from each Multi-Grid layer (blue) is shown together with the FWHM of the helium-3 tube (red), as a function of the distance from the Fermi-chopper. A linear fit (blue line) from the Multi-Grid points is also presented, demonstrating how the chopper pulse widens with distance. The fit uncertainties are presented as dashed lines.

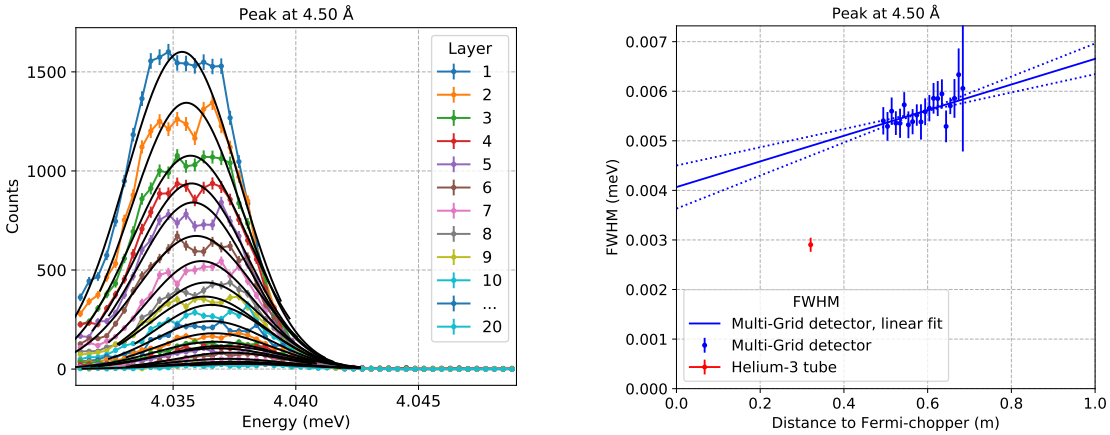

(a) **(b)**

Figure 86: At the left, the widening in energy is presented for each layer. The neutron energy distributions from each layer is fitted with a Gaussian (black) and the FWHM is extracted from the fit parameters. At the right, the FWHM from each Multi-Grid layer (blue) is shown together with the FWHM of the helium-3 tube (red), as a function of the distance from the Fermi-chopper. A linear fit (blue line) from the Multi-Grid points is also presented, demonstrating how the chopper pulse widens with distance. The fit uncertainties are presented as dashed lines.